RSC Advances

PAPER

View Article Online
View Journal | View Issue

Cite this: *RSC Adv.*, 2026, **16**, 25628

Effective degradation of carbofuran and organophosphate pesticides *via* a continuous-flow, visible-light-activated periodate oxidation system using floatable, sodium alginate/water lettuce-derived biochar/hollow glass microspheres

Karim Amer,[a] Arafat Toghan,[b] Emad M. Masoud,*[c] Magdi E. A. Zaki,[b] Hassan Shokry,[d] Mahmoud Samy[e] and Mohamed Mohamed Gaber *[d]

This study presents the synthesis of floatable sodium alginate/water lettuce-derived biochar/hollow glass microsphere (SA/WLBC/HGM) beads and their application as activators of periodate (PI) for the degradation of carbofuran (CBF) in a continuous-flow packed-bed photoreactor. The degradation mechanisms and the optimization of continuous-flow photoreactor systems remain insufficiently explored in the existing literature. Under the optimized conditions (catalyst dosage of 4 g, PI concentration of 0.8 g L^{-1}, flow rate of 2 mL min^{-1}, reaction time of 200 min, neutral pH, and ambient temperature), the SA/WLBC/HGMs–PI/light system achieved a CBF degradation efficiency of 94.11%. Under the same conditions, degradation efficiencies of 89.77, 84.50, and 78.12% were obtained for diazinon, malathion, and chlorpyrifos, respectively. Singlet oxygen species were the main contributors to the degradation process, and the degradation mechanism was explored. Toxic iodinated byproducts were not detected in the SA/WLBC/HGMs–PI/light degradation system, and most of the generated intermediates were less toxic compared to CBF. The SA/WLBC/HGMs beads demonstrated high stability under five successive cycles with a total loss of 1.86% in degradation efficiency. The degradation performance was evaluated in the presence of inorganic ions, natural organic matter, and different water matrices. Techno-economic analysis demonstrated the economic feasibility of the treatment system for mixed-pesticide wastewater, as evidenced by a relatively short payback period of 5.5 years, a positive net present value, and a profitability index exceeding unity. This study presents a stable, efficient, and inexpensive continuous-flow packed-bed photoreactor that can be employed for the remediation of real-world industrial effluents.

Received 29th March 2026
Accepted 29th April 2026

DOI: 10.1039/d6ra02593e

rsc.li/rsc-advances

1 Introduction

The use of pesticides to enhance agricultural productivity and the expansion of the agrochemical industry have resulted in the inevitable release of pesticides into streams.[1] Pesticides are toxic, persistent, and carcinogenic, threatening aquatic life and human health when they are disposed of in the environment without proper remediation.[2] Carbofuran (CBF), an *N*-methyl carbamate insecticide and nematicide, can be widely used due to its broad effectiveness in targeting pests. Thus, it can be found in different water matrices.[3] Ccanccapa *et al.* reported CBF with a concentration of 6.8 μg L^{-1} in river water in Spain.[4] CBF is bio-recalcitrant with high solubility (700 mg L^{-1}) and an extended half-life of up to 110 days, contaminating soil, groundwater, and nearby streams.[5] Furthermore, CBF can harm aquatic organisms and cause neurological damage in humans.[6] Therefore, it is critical to develop a treatment approach that can control the release of CBF into water sources.

Physical and chemical remediation approaches are not ideal for removing CBF due to their high energy consumption, modest performance, secondary pollution, and long reaction time.[7] Furthermore, biological methods cannot efficiently remove CBF due to its bio-resistance and complex structure.[8] Moreover, traditional treatment approaches cannot reduce CBF

[a]*Technology Management Department, Egypt-Japan University of Science and Technology (E-JUST), P.O. Box 179, New Borg El-Arab City Postal Code 21934, Alexandria, Egypt*

[b]*Chemistry Department, College of Science, Imam Mohammad Ibn Saud Islamic University (IMSIU), Riyadh 11623, Saudi Arabia*

[c]*Department of Chemistry, Faculty of Science, Islamic University of Madinah, Madinah 42351, Saudi Arabia. E-mail: emad.youssef@iu.edu.sa*

[d]*Environmental Engineering Department, Faculty of Engineering, Egypt-Japan University of Science and Technology (E-JUST), P.O. Box 179, New Borg El-Arab City Postal Code 21934, Alexandria, Egypt. E-mail: mohamed.gaber@ejust.edu.eg*

[e]*Public Works Engineering Department, Faculty of Engineering, Mansoura University, Mansoura 35516, Egypt*

concentration to the allowable limit (7 μg L^{-1}) according to International Union of Pure and Applied Chemistry guidelines.[9] Thus, a cheap, efficient treatment system is required to discharge CBF-laden wastewater into streams within the allowable limit.

Advanced oxidation processes (AOPs), such as photocatalysis and oxidant-based systems involving persulfate, peroxymonosulfate, hydrogen peroxide, and periodate (PI, IO_4^-) activation, have been extensively investigated for the removal of persistent pharmaceutical pollutants owing to their ability to generate highly reactive oxygen species (ROS).[10–12] Recent studies have extensively explored the photocatalytic degradation of CBF using semiconductor-based materials and engineered composites. For instance, ternary systems such as Y_2O_3/BaO/ZnO have demonstrated enhanced photocatalytic performance due to improved charge separation and reduced electron–hole recombination, achieving accelerated degradation kinetics under UV irradiation.[13] Similarly, a g–C_3N_4–based nanocomposite doped with transition V_2O_5 metal oxides has shown over 80% CBF degradation under visible light, attributed to favorable band alignment and increased generation of ROS.[14] Additionally, metal–organic framework (MOF)-based photocatalysts, such as Ni-doped MIL-125(Ti), have demonstrated significantly enhanced degradation performance, achieving up to ~82% CBF removal under optimized conditions.[15,16] These photocatalytic systems rely primarily on light-induced electron–hole pair generation, which subsequently leads to the production of ROS for pollutant degradation. Despite their promising performance, several limitations restrict the practical applicability of photocatalytic systems. These include rapid charge carrier recombination, reduced efficiency in turbid or real water matrices, catalyst deactivation, and the predominant use of batch-scale reactors under controlled laboratory conditions. In addition, post-treatment catalyst separation and recovery remain significant operational challenges.[15,16] In contrast to conventional photocatalysis, the present study employs light not as a primary driver for semiconductor excitation, but as an auxiliary activation source to enhance PI decomposition and ROS generation. Pristine biochar-based catalysts exhibit negligible intrinsic photocatalytic activity; instead, they function as efficient PI activators through surface-mediated redox interactions.[17,18] This distinction represents a fundamentally different degradation pathway compared to traditional photocatalytic systems.

PI has occupied a remarkable position among oxidants, such as hydrogen peroxide, persulfate, and peroxymonosulfate, for the degradation of emerging refractory pollutants due to its green nature, stability, and simple storage/transport.[19] Moreover, hydrogen peroxide, persulfate, and peroxymonosulfate have stronger steric hindrance and shorter O–O bond length compared to PI, which complicates the activation of these oxidants.[20] Additionally, iodine radicals (*e.g.*, periodyl radicals ($IO_4^{\bullet}$) and iodyl radicals ($IO_3^{\bullet}$)) with higher reactivity compared to the ROS produced in hydrogen peroxide, persulfate, and peroxymonosulfate-based degradation systems can be generated in PI-based AOPs.[21] PI without activation cannot effectively degrade organic pollutants owing to its limited oxidative potential (E_o = +1.6 V *vs.* NHE).[22] Thus, activation is needed to generate a series of ROS, such as iodine radicals, hydroxyl radicals ($^{\bullet}OH$), superoxide radicals ($O_2^{\bullet-}$), singlet oxygen ($^1O_2$), and $O(^3P)$.[23]

Periodate can be activated *via* an external energy source (*e.g.*, heat, UV) and/or a redox reaction using transition metals.[24,25] These activation approaches have some limitations for scalable applications, represented in their high energy consumption and possible leaching of metal ions into the treated solution. Thus, an environmentally friendly, inexpensive, and efficient activator must be adopted for the real-world applications of PI-based AOPs.

Biochar, a metal-free carbonaceous material with low cost, considerable surface area, and increasing surface functional groups, can be fabricated through the pyrolysis of organic biomass, such as sugarcane bagasse, rice husk, and banana peel, under an anoxic environment; therefore, it can serve as an activator for PI without energy consumption and secondary pollution.[26,27] Herein, water lettuce (WL) was valorized to biochar for employment in environmental remediation as a PI activator, contributing to managing WL instead of dumping it into landfill, which pollutes the environment.[28] Furthermore, the risks associated with the spread of WL in water streams, such as the complex penetration of sunlight and the deficit of dissolved oxygen in water sources, can be controlled through the conversion of WL to biochar.[29]

The real-world application of PI-based AOPs is still restricted due to the complex gathering of solid catalysts (*e.g.*, biochar) after treatment, the limited focus on the optimization of continuous-flow reactors, and worries related to the possible formation of iodinated disinfection byproducts (*e.g.*, IO_4^-, IO_3^-, I^-, I_2, I_3^-, and hypoiodous acid (HOI)). Zou *et al.* fabricated biochar-based alginate composite magnetic beads for the degradation of tetracycline hydrochloride *via* peroxymonosulfate activation in a bench-scale reactor.[30] Also, Abdul-Raheem *et al.* prepared alginate-based BiOBr/biochar composite beads as a photocatalyst for the degradation of ciprofloxacin in a bench-scale reactor.[31] Thus, in this study, a composite of sodium alginate (SA) and biochar was synthesized and loaded onto hollow glass microspheres (HGMs) to produce low-density, floatable beads, facilitating their flexible collection. The introduction of SA and HGMs enhances stability and increases the number of functional groups, thereby ameliorating the activation performance of the fabricated beads.[32,33]

Continuous-flow reactors introduce additional complexities, including hydrodynamic effects, mass transfer limitations, residence time distribution, and catalyst stability under prolonged operation.[34,35] These factors significantly influence degradation efficiency and process scalability but remain insufficiently addressed in the literature. Therefore, the development of an efficient continuous-flow degradation system would represent a critical advance beyond conventional batch approaches. The present work addresses this gap by integrating a floatable biochar-based catalytic system within a packed-bed continuous-flow photoreactor, enabling sustained operation, improved catalyst handling, and enhanced practical

applicability. The performance of the beads was systematically evaluated under various operating conditions to optimize the continuous-flow degradation of emerging pollutants. Additionally, herein, the transformation pathways of PI during the degradation process were monitored to investigate the possible generation of iodinated disinfection byproducts.

In this study, the fabricated floatable SA/water lettuce-derived biochar (WLBC)/HGMs beads were prepared, characterized, and employed as a PI activator in a continuous-flow packed-bed photoreactor for the degradation of CBF, diazinon, malathion, and chlorpyrifos. The degradation system was optimized under different operating parameters, such as pH, temperature, catalyst dose, time, and PI concentration. The main ROS, degradation mechanism, and degradation pathways were investigated. Additionally, the recyclability of the synthesized beads over multiple repeated runs was analyzed, the possible transformation of PI to iodinated disinfection byproducts was monitored, and the effects of inorganic ions, organic matter, and water matrices on the degradation performance were explored. Moreover, the profitability of the proposed degradation system was evaluated through a detailed techno-economic analysis.

2 Materials and methods

2.1. Materials

WL plants, utilized as the primary biomass precursor for biochar production in this study, were gathered from Mariout Lake, Alexandria, Egypt. Deionized water was employed throughout all experimental procedures. All chemicals utilized in this study were of analytical grade and applied directly, without any additional purification (Text S1).

2.2. Biochar synthesis

WLBC was synthesized from the collected water lettuce biomass *via* pyrolysis at 500 °C for 2 h under a nitrogen atmosphere. A detailed description of the preparation procedure is provided in Text S2 and presented in Fig. S1.

2.3. Fabrication of the composite beads

Initially, the SA solution was prepared by dissolving 6 g of SA in 200 mL of deionized water under continuous stirring (600 rpm) at 60 °C using a magnetic hotplate stirrer (MSH–20D, Daihan Scientific, Vietnam) until a homogeneous viscous solution was formed. After cooling to room temperature, WLBC (10 g) and HGMs (7 g) were gradually incorporated into the SA solution under stirring (100 rpm) to ensure uniform dispersion. The resulting suspension was dropped at a controlled flow rate (3 mL min^{-1}) into a 3% (w/v) $CaCl_2$ crosslinking solution using a peristaltic pump (Masterflex C/L 77120-62, 60 rpm, Cole-Parmer Instrument Company, Barrington, IL, USA), where ionic gelation occurred, forming stable beads.[36] The beads were allowed to harden in the $CaCl_2$ solution for 10 h to ensure complete crosslinking.[37,38] Thereafter, the produced SA/WLBC/HGMs beads were collected using a stainless-steel sieve, thoroughly washed to remove excess calcium ions, and dried at 65 °C (ED 53, Binder, Germany) before use. A schematic illustration outlining the complete synthesis of the composite beads is presented in Fig. S2.

2.4. Experimental configuration for CBF degradation

CBF degradation experiments were performed in a laboratory-scale packed-bed photoreactor (Fig. 1). The reactor consisted of a cylindrical column (inner diameter: 1.5 cm; height: 10 cm) made of quartz. The column was vertically oriented and equipped with two valves located at the top and bottom to regulate influent entry and effluent discharge. It was partially packed with a catalyst bed to a height of approximately 7.5 cm, corresponding to 25% of the total column height. The effective volume of the packed catalyst bed was 13.2 mL. To maintain fixed-bed operation and prevent particle fluidization during continuous flow, the catalyst layer was secured between two inert mesh screens positioned above and below the bed. The packed column was installed inside a closed wooden enclosure to ensure controlled irradiation conditions. This enclosure minimized interference from ambient light and reduced losses from light scattering. Illumination was provided by two 400 W metal halide lamps ($\lambda_{max} = 510$ nm), symmetrically positioned 15 cm from the column on opposite sides to ensure uniform light distribution across the catalyst bed. The CBF and PI stock solutions were stored in separate reservoirs located at a higher elevation than the reactor inlet to facilitate gravitational feeding and reduce energy consumption associated with pumping. Each reservoir was positioned on a digitally controlled magnetically stirred hotplate to ensure continuous mixing and simultaneous preheating of the influent solutions to the target reaction temperature before introducing them into the continuous system. In addition, each reservoir was fitted with an individual outlet tube and control valve, and the two streams were combined *via* a T-shape junction immediately before entering the reactor inlet to ensure controlled and homogeneous mixing before entry. The upward flow into the fixed-bed column was regulated using a peristaltic pump (Masterflex L/S Series (model: 07523-80), Cole-Parmer Instrument Company, Barrington, IL, USA) installed adjacent to the mixing junction at the same elevation as the reactor inlet. The distance between the mixing junction and the reactor inlet was deliberately minimized (approximately 30 cm, including the pump width) to restrict premature interaction between PI and CBF before contact with the catalyst bed. This configuration limited non-catalytic oxidation in the feed line and ensured that pollutant degradation was initiated predominantly within the irradiated catalytic zone of the reactor. The pH of both CBF and PI influent solutions was adjusted to the desired value using 1 M H_2SO_4 and/or 1 M NaOH before introducing the solutions into the continuous system.

2.5. Experimental procedures

To initiate CBF degradation in the continuous packed-bed photoreactor, the bottom inlet valve of the column was opened first, followed by the junction valve, allowing the pre-mixed influent stream to flow upward into the reactor from the base

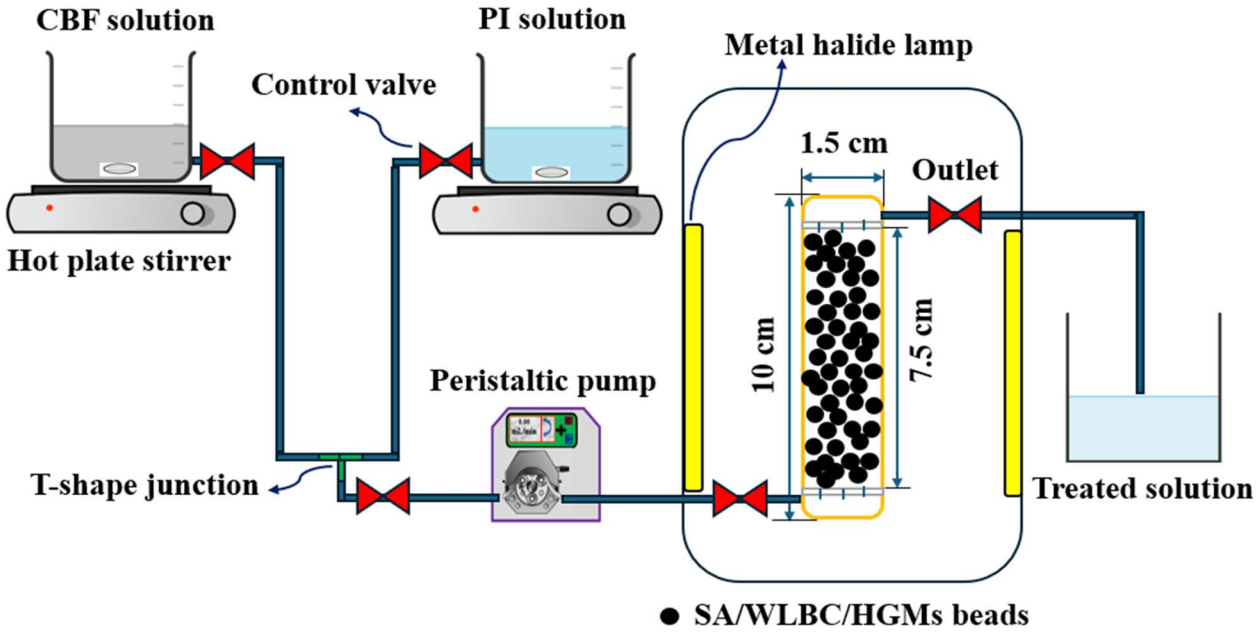

Fig. 1 Configuration of the laboratory-scale continuous-flow packed-bed photoreactor system.

of the column. The system was operated until the packed bed was fully saturated with the influent solution. Subsequently, the light source was switched on to induce PI photoactivation. Thereafter, the top valve of the column was opened to permit the outflow of the treated effluent into the effluent tank. Effluent samples were collected from the reactor outlet at fixed time intervals and immediately quenched with 60 μL of 1 M $Na_2S_2O_3$ solution before analysis. The added sodium thiosulfate can rapidly scavenge residual oxidizing species, thereby terminating the ongoing oxidation reactions and preventing further degradation of the target compounds after sampling.[39] All experiments were conducted in triplicate, and the reported data represent the mean values, while the error bars in the corresponding figures denote the standard deviation. The removal efficiency for CBF was calculated according to Table S1, eqn (1). Kinetic analyses were subsequently conducted using the pseudo-first-order (Table S1, eqn (2)) and pseudo-second-order (Table S1, eqn (3)) models to identify the model that most accurately describes the degradation behavior of CBF under the investigated experimental conditions.[40]

The effects of key operating parameters on CBF degradation were systematically evaluated by varying one factor at a time while keeping the others constant. The parameters investigated included reaction temperature, initial solution pH, hydraulic flow rate, catalyst dosage, PI concentration, initial CBF concentration, and reaction time. The optimal conditions determined from these experiments were subsequently applied in all further investigations.

To elucidate the oxidation mechanism, radical quenching experiments were conducted using selective scavengers to identify the dominant ROS responsible for CBF degradation. Furfuryl alcohol, chloroform, and *tert*-butyl alcohol were employed as selective quenchers for $^1O_2$, $O_2^{\bullet-}$, and $^{\bullet}OH$, respectively.[41–43] Phenol was employed as a scavenger for $IO_4^{\bullet}$, $IO_3^{\bullet}$, and $^{\bullet}OH$ radicals,[43] while KI targeted both $IO_3^{\bullet}$ and $^{\bullet}OH$ radicals.[44] Additionally, 2-propanol was used to scavenge both $^{\bullet}OH$ and $O(^3P)$.[45] Based on these experiments, a plausible degradation mechanism involving iodine-centered radicals and other ROS was proposed, including their interconversion pathways under light irradiation.

The environmental implications of the SA/WLBC/HGMs–PI/light system were evaluated by systematically monitoring the generation and transformation of all relevant iodine species during CBF oxidation, including IO_4^-, IO_3^-, I^-, I_2, I_3^-, and HOI. In addition, the degradation intermediates were identified to elucidate the plausible transformation pathways. Subsequently, a toxicological assessment was conducted to evaluate the potential ecological risks associated with the treated effluents by predicting the acute toxicity of CBF and its identified transformation intermediates using the Toxicity Estimation Software Tool (T.E.S.T.).

The practical applicability of the system was evaluated through recyclability experiments, in which the same batch of SA/WLBC/HGMs composite beads was reused over multiple consecutive cycles. In addition, the influence of common inorganic anions (HCO_3^-, NO_3^-, SO_4^{2-}, Cl^-, and HPO_4^{2-}) and natural organic matter (NOM) (*e.g.*, humic acid (HA)) was examined to evaluate system robustness under realistic water conditions. Performance validation was also conducted using various real water matrices, including tap, river, lake, and seawater samples. Furthermore, the degradation performance of the proposed system was assessed for degrading other pesticides besides CBF, such as diazinon, malathion, and chlorpyrifos. These experiments were conducted using both individual pesticide solutions and mixed-pesticide wastewater to comprehensively evaluate the versatility and applicability of

the developed treatment process. Finally, techno-economic feasibility was assessed to evaluate the potential of the system for practical large-scale wastewater treatment applications.

2.6. Characterization and analytical methods

The physicochemical properties of the SA/WLBC/HGMs beads were comprehensively characterized using multiple analytical techniques, including X-ray diffraction (XRD), Fourier transform infrared spectroscopy (FTIR), scanning electron microscopy (SEM), transmission electron microscopy (TEM), energy-dispersive X-ray spectroscopy (EDX), Brunauer–Emmett–Teller (BET) surface area analysis, and the Barrett–Joyner–Halenda (BJH) method for pore size distribution. The specific roles and instrumental details of each characterization technique are provided in detail in Text S3.

The analytical methodologies employed in this study are described in detail in Text S4 and Table S2, which provide comprehensive information on the instrumentation, experimental procedures, and operating conditions used throughout the analyses.

3 Results and discussion

3.1. Physicochemical characterization of the SA/WLBC/HGMs beads

The XRD diffractogram of the synthesized SA/WLBC/HGMs beads is presented in Fig. 2a. At low diffraction angles, the peak at $2\theta = 21.8°$ is assigned to the (101) plane of silicon dioxide (SiO_2, ICSD 01-076-0941). The presence of SiO_2 originates mainly from the silica-rich HGMs. In addition, a portion of the detected SiO_2 may also arise from mineral-containing soil particles that were associated with the collected biomass.[46] The reflection at 24.48° is attributed to the (012) crystallographic plane of calcium carbonate ($CaCO_3$, JCPDS 00-001-0837), together with the (111) plane of potassium chloride (KCl, ICSD 01-075-0296). The formation of $CaCO_3$ can be attributed to multiple processes occurring during material preparation. During bead gelation and subsequent drying, Ca^{2+} ions undergo partial carbonation, leading to the precipitation of $CaCO_3$. Additionally, carbonate species may also develop during the pyrolysis stage, where CO_2 released from thermal decomposition becomes retained within the matrix and subsequently reacts with calcium-bearing phases, further contributing to the formation of $CaCO_3$.[47] The detected KCl phase is associated with naturally occurring potassium salts present in the water lettuce biomass that remain within the biochar matrix after thermal treatment. The formation of KCl may also be facilitated during the bead preparation stage through ionic interactions occurring in the $CaCl_2$ crosslinking solution, where chloride ions can combine with potassium species released from the biomass-derived components. The band at 27.24° corresponds to the (111) and (002) lattice planes of CaS (PDF 00-008-0464) and carbon (C, JCPDS 00-041-1487), respectively. The presence of CaS can be attributed to the transformation of sulfur-containing mineral residues inherently associated with the collected biomass. During pyrolysis, the high-temperature and oxygen-

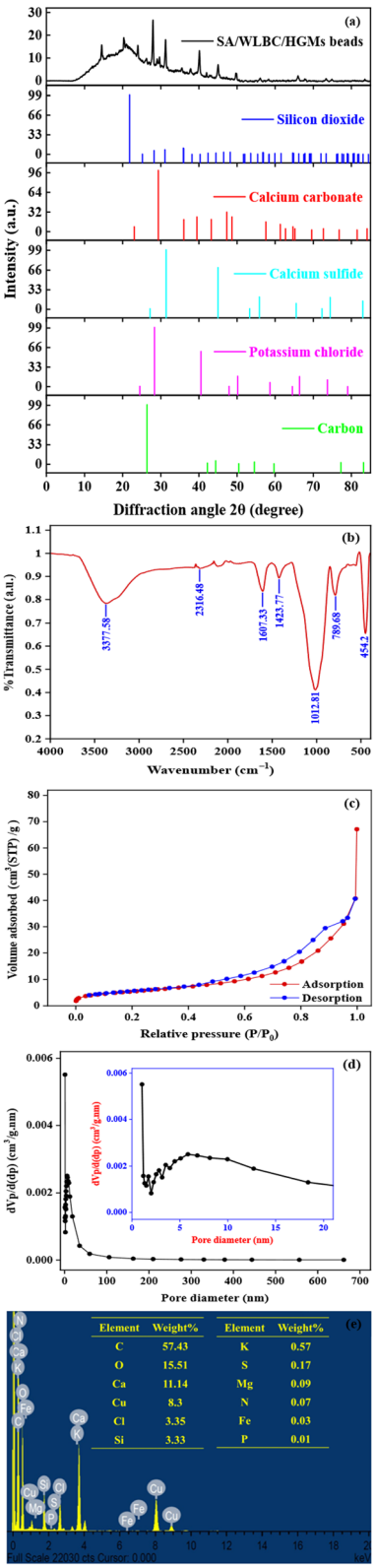

Fig. 2 (a) XRD diffractogram, (b) FTIR spectrum, (c) adsorption–desorption isotherms, (d) pore size distribution (inset: magnified view within the 1–20 nm range), and (e) EDX spectrum of the synthesized SA/WLBC/HGMs beads.

limited environment promote the reduction of both organically bound and inorganic sulfur species. These reduced sulfur species can subsequently react with calcium-bearing components, resulting in the formation of thermodynamically stable CaS phases.[48,49] The carbon-related peaks are attributed mainly to the incorporated WLBC generated after the pyrolysis of the water lettuce biomass. The diffraction signal at 28.26° arises from the combined contributions of SiO_2 (111) and KCl (200), whereas the peak at 29.34° is assigned to $CaCO_3$ (104). The reflection at 31.26° is attributed to overlapping planes of SiO_2 (102) and CaS (200), while the band at 35.94° is ascribed to the SiO_2 (200) plane. Furthermore, the diffraction signal at 36.1° corresponds to contributions from SiO_2 (112) and $CaCO_3$ (110), while the peak at 38.13° is assigned to the SiO_2 (201) plane. The diffraction peak at 40.66° belongs to overlapping contributions from the (210) plane of SiO_2, the (113) plane of $CaCO_3$, and the (220) plane of KCl. The reflection observed at 42.33° is attributed to the (211) crystallographic plane of SiO_2, together with the (100) plane of carbon. In addition, the band at 43.25° corresponds to the (202) plane of $CaCO_3$. Moreover, the diffraction signal at 44.38° arises from the combined contributions of the (202) plane of SiO_2, the (220) plane of CaS, and the (101) plane of carbon. The peak at 47.66° is attributed to overlapping reflections of SiO_2 (113), $CaCO_3$ (024), and KCl (311). Similarly, the band located at 48.42° corresponds to the (212) plane of SiO_2 together with the (116) plane of $CaCO_3$. The reflection signal at 50.24° is attributed to the (220) plane of SiO_2, overlapping with KCl (222) and carbon (102). The peak observed at 56.78° is associated with the (301) plane of SiO_2, along with contributions from CaS (222) and carbon (005). The diffraction signal at 58.57° arises from the combined reflections of SiO_2 (222), $CaCO_3$ (122), KCl (400), and carbon (103). At higher diffraction angles, the peak at 64.78° is assigned to overlapping planes of SiO_2 (204), $CaCO_3$ (300), KCl (331), and CaS (400). The signal at 67.55° corresponds to the (320) plane of SiO_2 together with KCl (420). The peak located at 73.32° is attributed to the combined contributions of SiO_2 (322), $CaCO_3$ (128), KCl (422), and CaS (331). Finally, the diffraction signal at 74.52° corresponds to the (420) crystallographic plane of CaS. The diffraction peaks and their corresponding Miller indices (*hkl*) are summarized in Table S3. The coexistence of SiO_2, $CaCO_3$, KCl, CaS, and carbon phases indicates that the silica-based HGMs, biomass-derived carbon, and calcium-containing mineral species were successfully incorporated into the alginate matrix, confirming the effective synthesis of the SA/WLBC/HGMs composite beads.

The FTIR spectrum (Fig. 2b) of the synthesized SA/WLBC/HGMs beads confirms the successful integration of the three components through the presence of characteristic functional groups. The broad peak at 3377.58 cm^{-1} corresponds to O–H stretching vibrations, which may originate from hydroxyl groups in the biochar and alginate. Similar O–H bands were reported at 3454 cm^{-1} for lettuce-waste-derived biochar activated with H_3PO_4,[50] at 3435 cm^{-1} for water hyacinth biochar,[51] at 3300 cm^{-1} for cauliflower-derived biochar,[52] and at 3415.61 cm^{-1} for biochar from water lettuce plants.[53] The peak at 2316.48 cm^{-1} is attributed to alginate-related vibrations, consistent with the band observed at 2358.6 cm^{-1} in alginate-based biochar composite beads.[54,55] The absorption band at 1607.33 cm^{-1} can be assigned to multiple functional groups. It may correspond to O–H bending vibrations, like the peaks at 1641 cm^{-1} in lettuce-waste biochar,[50] and 1624.45 cm^{-1} in water lettuce biochar.[53] Additionally, this band may be attributed to C=C and C=O stretching vibrations of aromatic structures in biochar, as reported at 1618 cm^{-1} for water hyacinth biochar,[51] and at 1698 cm^{-1} for bamboo leaf biochar.[56] Furthermore, it may correspond to the asymmetric stretching vibrations of COO^- groups in alginate, which were identified at 1600 cm^{-1} in magnetic biochar crosslinked composite beads,[57,58] and at 1630 cm^{-1} in alginate-based BiOBr/biochar composite beads.[31] The band at 1423.77 cm^{-1} may be assigned to $-CH_2$ bending vibrations, consistent with peaks at 1429.14 cm^{-1} for water lettuce biochar,[53] 1368 cm^{-1} for water lettuce biochar,[56] and 1420 cm^{-1} for water hyacinth biochar.[51] This band may also correspond to the symmetric stretching vibrations of COO^- groups in alginate, as reported at 1410 cm^{-1} in magnetic biochar aluminum crosslinked composite beads,[57] 1401 cm^{-1} in alginate-based BiOBr/biochar composite beads,[31] and 1415.6 cm^{-1} in alginate-based biochar composites.[54] The peak at 1012.81 cm^{-1} is attributed to C–O stretching vibrations, like those observed at 1078 cm^{-1} for bamboo leaf biochar,[56] 1045.04 cm^{-1} for water lettuce biochar,[53] and 1056 cm^{-1} for water hyacinth biochar.[51] The band at 789.68 cm^{-1} corresponds to O–C–O or alginate–O vibrations in alginate, comparable to the peak at 795.5 cm^{-1} reported for alginate-based biochar composites.[54,55] Finally, the absorption peak at 454.2 cm^{-1} is assigned to Si–O–Si and Si–O bending vibrations, confirming the presence of HGMs within the composite matrix. A similar band at 479 cm^{-1} was reported for polyaniline/silicon dioxide nanocomposites.[59] The FTIR spectral bands of SA/WLBC/HGMs beads and corresponding functional group assignments based on literature reports are summarized in Table S4. Overall, the coexistence of these functional groups confirms the successful synthesis and integration of SA, WLBC, and HGMs into a unified composite structure, providing abundant reactive sites and structural stability suitable for PI activation and CBF degradation.

The adsorption–desorption isotherms (Fig. 2c) and pore size distribution (Fig. 2d) of the SA/WLBC/HGMs beads demonstrate their suitability for heterogeneous PI activation. The beads exhibited a specific surface area (S_{BET}) of 19.822 $m^2\ g^{-1}$ and a total pore volume of 0.0616 $cm^3\ g^{-1}$, indicating the presence of a moderately developed porous structure. The accessible surface area and interconnected pore network improve reactant transport and minimize diffusion limitations under continuous-flow conditions.[60] The micropore area (27.246 $m^2\ g^{-1}$) and micropore volume (0.0667 $cm^3\ g^{-1}$) suggest that microporosity contributes significantly to the overall surface characteristics, providing abundant active sites for adsorption and surface-mediated reactions.[61] The average pore diameter of 9.7863 nm falls within the mesoporous range, which is advantageous for facilitating mass transfer and diffusion of PI ions and CBF molecules into the internal structure of the beads. Such a hierarchical pore structure, combining micropores and

mesopores, enhances the adsorption of CBF and promotes intimate contact between the pollutant and ROS generated from PI activation.[62] Consequently, these favorable textural features contribute to efficient PI activation and sustained catalytic performance during CBF degradation in the fixed-bed photoreactor system.

The EDX spectrum of the SA/WLBC/HGMs composite beads (Fig. 2e) reveals that carbon (57.43 wt%) and oxygen (15.51 wt%) are the predominant elements, originating mainly from the SA matrix and the biochar framework. These components can provide abundant surface functional groups and electron-rich domains that facilitate PI adsorption and promote electron transfer, thereby accelerating ROS generation and facilitating PI activation.[63,64] Calcium (11.14 wt%) is attributed primarily to the crosslinking of SA with Ca^{2+}, forming a stable hydrogel network that enhances mechanical strength and structural integrity under continuous-flow conditions.[38] In addition, calcium can enhance PI activation by promoting the electrostatic adsorption of negatively charged PI onto surface-bound Ca^{2+} sites, thereby increasing interfacial contact, accelerating ROS generation, and improving overall activation efficiency.[65] Copper (8.3 wt%) was also detected in the EDX analysis; however, this signal is most likely attributed to the copper grid used during sample preparation and measurement. Chlorine (3.35 wt%) may originate from calcium chloride used during bead crosslinking, while silicon (3.33 wt%) is derived mainly from the HGMs. Minor elements, including potassium (0.57 wt%), sulfur (0.17 wt%), magnesium (0.09 wt%), nitrogen (0.07 wt%), iron (0.03 wt%), and phosphorus (0.01 wt%), are associated primarily with the intrinsic mineral content of the biochar precursor. These heteroatoms can introduce surface defects and additional catalytic sites, thereby enhancing electron transfer processes and synergistically promoting PI activation.[66] The elemental mapping images of the synthesized beads (Fig. S3) further confirm the relatively uniform distribution of C, O, Ca, Cu, Cl, Si, and other trace elements (K, S, Mg, N, Fe, P) across the bead matrix, indicating successful integration of the composite constituents.

Fig. 3a presents SEM micrographs of the synthesized SA/WLBC/HGMs beads, revealing predominantly spherical and well-defined particles with relatively smooth external surfaces and slight textural roughness attributed to the incorporation of the biochar. The beads display a relatively uniform size distribution, with measured diameters ranging from approximately 25 to 44.5 μm with an average diameter of about 35.9 μm. This narrow size range indicates effective control during the process of bead fabrication and reflects the consistency of the synthesis method. At lower magnification, the beads appear densely packed with low agglomeration, which is advantageous for their application in a continuous-flow fixed-bed reactor, as it promotes homogeneous flow distribution and reduces channeling. The rough surface and porous texture, imparted by WLBC and HGMs, provide abundant active sites and enhanced interfacial contact for PI activation. These structural features facilitate electron transfer processes and improve oxidant accessibility, thereby enhancing CBF degradation efficiency.[67] The presence of fractured or partially collapsed beads can be attributed to internal stress generated during Ca^{2+}-mediated alginate crosslinking, drying-induced shrinkage, and heterogeneous interfacial bonding between the polymer matrix, WLBC, and HGMs.[36] Despite minor fractures, the overall spherical morphology and structural integrity support efficient mass transfer, oxidant diffusion, and catalytic stability under continuous-flow conditions.

The TEM micrographs of the SA/WLBC/HGMs composite beads at different magnifications (10 000–100 000×) are presented in Fig. 3b. The images reveal a well-defined hierarchical structure composed of uniformly distributed spherical domains embedded within a relatively translucent matrix. The dark, electron-dense spherical particles correspond to HGMs, which are homogeneously dispersed throughout the SA matrix, while the lighter, irregular regions are attributed to the WLBC phase. The spheres exhibit smooth surfaces and clear boundaries, confirming the structural integrity of the composite. The structural stability and homogeneous internal architecture of the composite beads ensure sustained catalytic activity and mechanical robustness under continuous-flow conditions, thereby enhancing the efficient degradation of CBF.[36,55]

The high-resolution TEM (HRTEM) image of the SA/WLBC/HGMs composite beads (Fig. S4a) reveals well-defined and regularly arranged lattice fringes, confirming the presence of crystalline domains within the composite matrix. The measured interplanar spacing (*d*-spacing) of approximately 0.33 nm is characteristic of graphitic carbon structures and indicates the presence of ordered carbon layers within the WLBC phase. The lattice fringe intensity profile extracted from the selected region (Fig. S4b) exhibits periodic oscillations with uniform peak-to-peak distances, further confirming the calculated lattice spacing and confirming the high degree of structural ordering. The clear and continuous fringes suggest good crystallinity and strong interfacial integration between the composite constituents, without noticeable structural disruption during synthesis. Such structural features are highly beneficial for PI activation in a continuous-flow fixed-bed photoreactor. The presence of graphitic domains with a 0.33 nm spacing facilitates electron transfer processes, which are essential for activating PI through radical and non-radical pathways.[67] Moreover, the stable crystalline framework contributes to the mechanical robustness and long-term catalytic stability of the beads under continuous-flow operation.[68,69]

3.2. Impact of reactor operating parameters on CBF degradation

The effects of key operational parameters on CBF degradation were systematically investigated, including temperature, pH, flow rate, catalyst dosage, PI concentration, and initial CBF concentration. A summary of these parameters and their corresponding conditions is provided in Table S5.

3.2.1. Reaction temperature. Temperature effects on the catalytic activity of the SA/WLBC/HGMs–PI/light system were systematically investigated by varying the reaction temperature from 25 to 65 °C. All experiments were conducted under identical operating conditions, including an initial CBF concentration of 15 mg L^{-1}, a catalyst dosage of 4 g, a PI concentration of 0.8 g L^{-1}, a constant influent flow rate of 2 mL min^{-1}, and

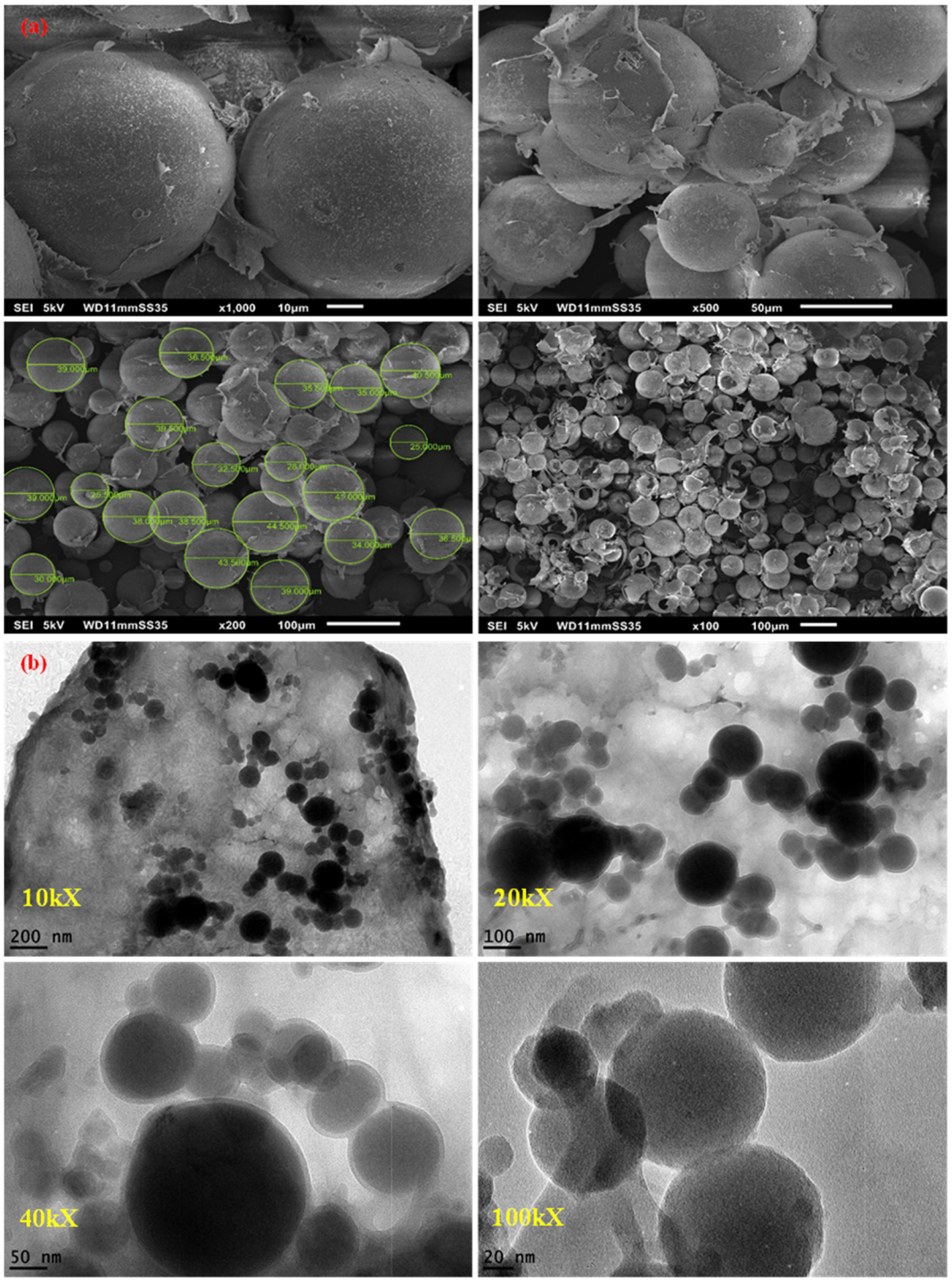

Fig. 3 (a) SEM micrographs and (b) TEM images of the SA/WLBC/HGMs beads at varying magnification levels.

neutral pH (pH 7). As illustrated in Fig. 4a, CBF removal efficiency increased with increasing temperature, reaching 94.25%, 96.76%, 98.78%, 99.62%, and 99.89% after 300 min at 25, 35, 45, 55, and 65 °C, respectively. The observed enhancement can be attributed to accelerated PI activation, increased generation of ROS, and more frequent effective interactions between CBF molecules and reactive radicals at elevated temperatures.[70] In addition, the results revealed that the overall increase in CBF removal efficiency from 25 to 65 °C was limited to approximately 5.6%. Therefore, to consider treatment efficiency and energy consumption, subsequent experiments were performed at 25 °C (ambient temperature), which provided high degradation performance while ensuring operational and economic feasibility for practical applications in wastewater treatment.

To further elucidate the degradation behavior of CBF under different temperature conditions, kinetic analyses were

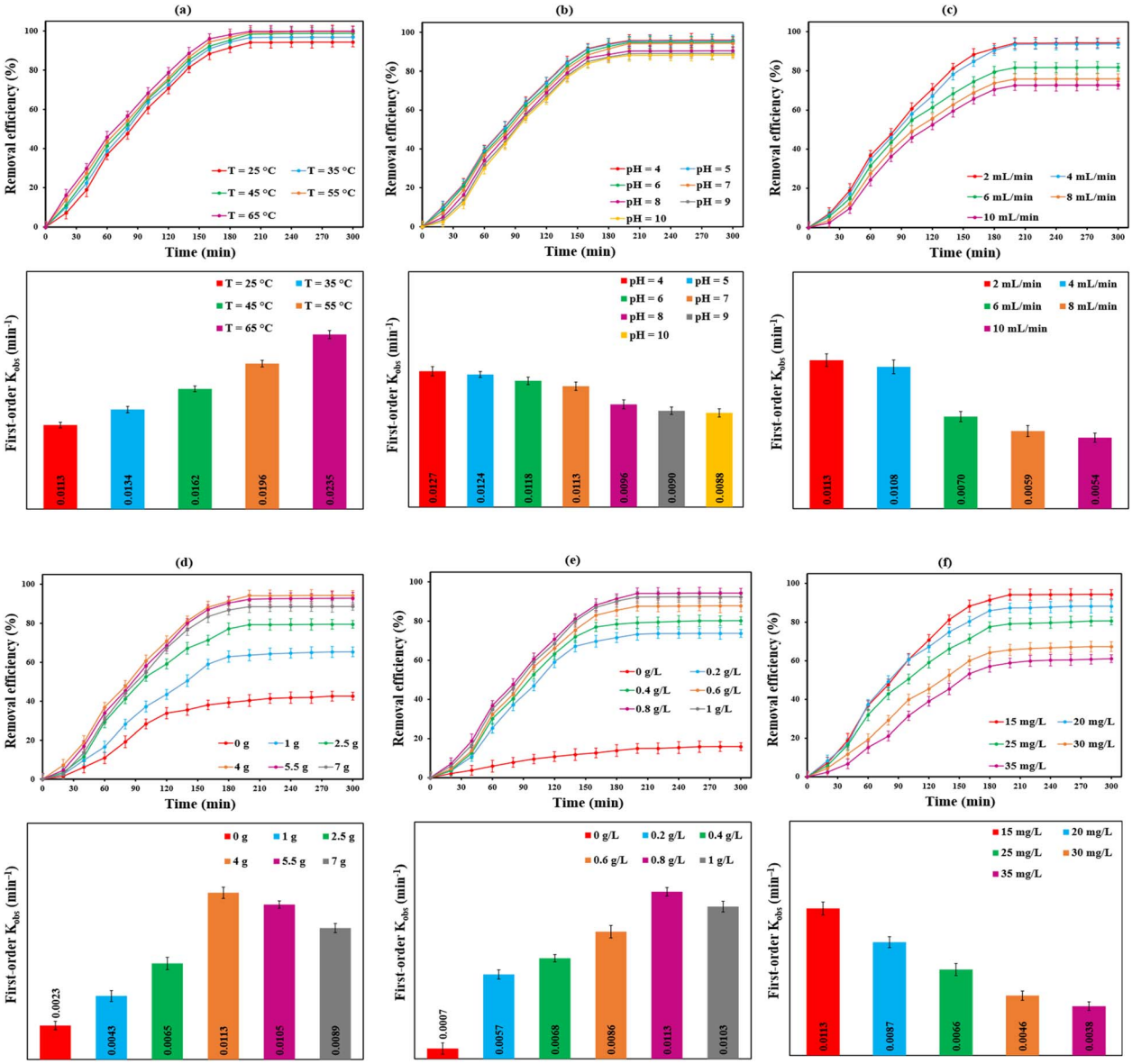

Fig. 4 CBF removal efficiency and corresponding pseudo-first-order rate constants within the SA/WLBC/HGMs–PI/light system at different (a) reaction temperatures, (b) solution pH, (c) input flow rates, (d) catalyst doses, (e) initial PI concentrations, and (f) initial CBF concentrations. Conditions: $[catalyst]_o$ = 4 g, $[PI]_o$ = 0.8 g L^{-1}, T = 25 °C, input flow rate = 2 mL min^{-1}, pH = 7, and $[CBF]_o$ = 15 mg L^{-1}.

conducted using both pseudo-first-order and pseudo-second-order models. For the pseudo-first-order model, the observed rate constants (K_{obs}) were 0.0113 (R^2 = 0.9785) min^{-1} at 25 °C, 0.0134 (R^2 = 0.9779) min^{-1} at 35 °C, 0.0162 (R^2 = 0.978) min^{-1} at 45 °C, 0.0196 (R^2 = 0.9735) min^{-1} at 55 °C, and 0.0235 (R^2 = 0.9642) min^{-1} at 65 °C (Fig. S5a). These results demonstrate a systematic increase in the reaction rate with rising temperature, which is consistent with the observed enhancement in CBF removal efficiency at elevated temperatures. For the pseudo-second-order model, the corresponding rate constants were 0.0021 (R^2 = 0.9512) L mg^{-1} min at 25 °C, 0.0035 (R^2 = 0.9197) L mg^{-1} min at 35 °C, 0.008 (R^2 = 0.8639) L mg^{-1} min at 45 °C, 0.0223 (R^2 = 0.7915) L mg^{-1} min at 55 °C, and 0.0612 (R^2 = 0.7649) L mg^{-1} min at 65 °C (Fig. S5b). The results revealed that the pseudo-first-order model generally exhibited higher and more consistent correlation coefficients across the entire range of reaction temperatures. Therefore, CBF degradation in the SA/WLBC/HGMs–PI/light system is best described by pseudo-first-order kinetics, which were consequently employed to analyze all subsequent experimental data.

The apparent activation energy (E_a) for CBF degradation in the SA/WLBC/HGMs–PI/light system was calculated using the Arrhenius equation, as described in our previous studies.[53,65] The estimated E_a value was 15.43 kJ mol^{-1} (Fig. S6), which is considerably lower than those reported for other biochar/alginate composite beads.[69,71] This relatively low activation energy reflects a reduced kinetic barrier, enabling efficient degradation under mild conditions with minimal thermal

energy input. Consequently, the SA/WLBC/HGMs–PI/light system exhibits strong potential for practical wastewater treatment and suitability for large-scale applications.

3.2.2. Initial solution pH. Variations in pH can markedly influence the degradation efficiency of organic micropollutants during AOPs.[72,73] To evaluate the pH adaptability and operational robustness of the SA/WLBC/HGMs–PI/light system, the initial solution pH was systematically adjusted to 4, 5, 6, 7, 8, 9, and 10. The experimental conditions were an initial CBF concentration of 15 mg L^{-1}, a catalyst dosage of 4 g, a PI concentration of 0.8 g L^{-1}, an input flow rate of 2 mL min^{-1}, and ambient temperature, with an experimental duration of 300 min. As illustrated in Fig. 4b, the CBF removal efficiencies were 95.85, 95.48, 94.84, 94.25, 90.41, 89.07, and 88.27% at pH values of 4, 5, 6, 7, 8, 9, and 10, respectively, while the respective first-order K_{obs} values were 0.0127, 0.0124, 0.0118, 0.0113, 0.0096, 0.009, and 0.0088 min^{-1}. The results revealed that only a modest decline of approximately 7.5% in removal efficiency was observed across this broad pH range, demonstrating the excellent resistance of the SA/WLBC/HGMs–PI/light system to fluctuations in pH. This high pH tolerance is particularly advantageous for sustainable water treatment applications, where influent pH conditions may vary considerably. Despite maintaining high catalytic activity over a broad pH range, the SA/WLBC/HGMs–PI/light system exhibits a clear pH-dependent behavior, with maximal CBF degradation under acidic conditions and a gradual decline in efficiency as the pH increases. Similar observations have been reported for biochar-based PI catalytic oxidation systems,[20] demonstrating effective degradation of sulfamethazine and diclofenac sodium, respectively. Under acidic conditions, the abundance of protons enhances interfacial electron-transfer processes on the catalyst surface, thereby promoting the generation of highly reactive $IO_3^{\bullet}$ and accelerating pollutant oxidation.[74] As the pH shifts to neutral and alkaline ranges, periodate increasingly transforms from the highly oxidative IO_4^- species (E_o = +1.6 V *vs.* NHE) into less reactive polymeric or proton-deficient forms such as $H_2I_2O_{10}^{4-}$ with a markedly lower redox potential (E_o = + 0.7 V *vs.* NHE). This speciation shift reduces the overall oxidizing strength of the PI-based system, restricts ROS formation, and consequently leads to a slight reduction in CBF degradation efficiency at elevated pH values.[75,76] The neutral condition was identified as optimal, as the difference in CBF removal between neutral pH and the maximum degradation achieved under acidic conditions was negligible (<1.6%). Operating at neutral pH eliminates the need for pH adjustment, reducing chemical consumption and operational costs and enhancing the practical and economic feasibility of the system.

3.2.3. Flow rate. To achieve an optimal balance between pollutant mass transfer and catalytic system stability, the hydraulic flow rate was systematically optimized. Experiments were conducted under fixed operational conditions (initial CBF concentration = 15 mg L^{-1}, catalyst dosage = 4 g, PI concentration = 0.8 g L^{-1}, neutral pH, and ambient temperature), with the influent flow rate varied from 2 to 10 mL min^{-1} using a peristaltic pump. As illustrated in Fig. 4c, CBF removal efficiency in the SA/WLBC/HGMs–PI/light system exhibited a pronounced dependence on flow rate. Effective CBF degradation was achieved across all tested conditions; however, substantially higher removal efficiencies were observed at lower flow rates. Specifically, flow rates of 2 and 4 mL min^{-1} resulted in CBF removal efficiencies of 94.25 and 93.65%, respectively, after 300 min of operation. This enhanced performance can be primarily attributed to the prolonged hydraulic residence time, which facilitated sustained interactions among CBF molecules, the PI, SA/WLBC/HGMs beads, and light irradiation. Such conditions favor continuous radical chain reactions and promote the generation and utilization of ROS, thereby enhancing oxidative degradation.[77,78] In contrast, increasing the flow rate from 6 to 10 mL min^{-1} led to a gradual decline in CBF removal efficiency, decreasing to 81.76, 76.04, and 72.77%, respectively. The diminished performance at higher flow rates is likely to be due to reduced contact time and insufficient ROS production caused by shortened hydraulic retention, which limits effective oxidation.[79] To further elucidate this behavior, kinetic analyses were performed using the pseudo-first-order model (Fig. 4c), revealing a systematic decrease in pseudo-first-order rate constants from 0.0113 (R^2 = 0.9785) min^{-1} at 2 mL min^{-1} to 0.0108 min^{-1}, 0.007 min^{-1}, 0.0059 min^{-1}, and 0.0054 min^{-1} at 4, 6, 8, and 10 mL min^{-1}, consistent with the observed decline in the CBF degradation efficiency at higher flow rates. Considering both degradation efficiency and operational stability, a flow rate of 2 mL min^{-1} was therefore selected as optimal for subsequent experiments.

3.2.4. Catalyst dosage. Optimizing the catalyst dosage is crucial for maximizing oxidant activation and pollutant degradation efficiency while avoiding unnecessary material consumption and adverse radical interactions.[68] Fig. 4d presents the influence of dosage of SA/WLBC/HGMs composite beads (0–7 g) on CBF degradation efficiency and reaction kinetics. The experimental results demonstrate that, in the absence of beads (0 g), the PI/light system exhibited limited catalytic activity, achieving only 42.55% CBF removal with an apparent first-order K_{obs} of 0.0023 min^{-1} after 300 min under an initial CBF concentration of 15 mg L^{-1}, a PI concentration of 0.8 g L^{-1}, neutral pH, ambient temperature, and an input flow rate of 2 mL min^{-1}. Upon the introduction of SA/WLBC/HGMs beads, CBF degradation in the SA/WLBC/HGMs–PI/light system exhibited strong dependence on catalyst dosage. The addition of 1 g and 2.5 g of beads enhanced the CBF removal efficiencies and the accompanying first-order rate constants to 65.53% (0.0043 min^{-1}) and 79.53% (0.0065 min^{-1}). Further increasing the catalyst dosage to 4 g resulted in a maximum CBF removal efficiency of 94.25%, with a corresponding pseudo-first-order K_{obs} value of 0.0113 min^{-1}. The enhancement in system performance with increasing catalyst dosage can be attributed primarily to the enlarged surface area and the higher density of reactive sites (*e.g.*, oxygen-containing functional groups) available for pollutant–catalyst interactions. These characteristics promote more efficient PI activation and subsequent generation of ROS, thereby accelerating the oxidative degradation of CBF.[80] Further increasing the catalyst loading to 5.5 g and 7 g resulted in slight decreases in CBF removal efficiencies and the corresponding first-order rate constants, reaching 92.79%

(0.0105 min^{-1}) and 88.71% (0.0089 min^{-1}), respectively. Considering the maximum CBF removal efficiency obtained at a catalyst dosage of 4 g, together with practical considerations such as cost efficiency, 4 g was determined to be the optimal catalyst dosage.

3.2.5. PI concentration. The effect of PI concentration (0–1 g L^{-1}) on CBF decomposition in the SA/WLBC/HGMs–PI/light system was systematically investigated under fixed operating conditions (CBF = 15 mg L^{-1}, bead dosage = 4 g, pH = 7, T = 25 °C, and flow rate = 2 mL min^{-1}), as shown in Fig. 4e. The findings indicate that, in the absence of PI (0 g L^{-1}), the SA/WLBC/HGMs–PI/light system displayed weak catalytic performance, resulting in a CBF removal efficiency of only 15.94% and a low apparent pseudo-first-order rate constant of 0.0007 min^{-1}. At relatively low PI concentrations (0.2 and 0.4 g L^{-1}), the CBF removal efficiencies and first-order K_{obs} values reached 73.8% (0.0057 min^{-1}) and 80.3% (0.0068 min^{-1}), respectively, after 300 min. Further increasing the PI concentration to 0.6 and 0.8 g L^{-1} led to a pronounced enhancement in CBF removal efficiencies, reaching 87.9 and 94.25%, along with corresponding increases in the pseudo-first-order rate constants to 0.0086 and 0.0113 min^{-1}. This enhancement can be attributed to the increased generation of ROS arising from more efficient PI activation, as well as improved compatibility between the number of catalytically active sites and the availability of IO_4^- ions, which collectively promote CBF degradation.[81] However, when the PI dosage was further increased to 1 g L^{-1}, a slight decline in CBF removal efficiency was observed (92.37%), along with a reduction in the corresponding first-order K_{obs} value to 0.0103 min^{-1}. This behavior is likely to be associated with excessive PI concentration, inducing mutual quenching reactions among reactive species and the formation of less reactive oxidative intermediates, thereby diminishing the effective ROS concentration available for pollutant degradation (Table S6, eqn (1)–(6)).[80,82] Considering overall degradation performance, environmental sustainability, and economic feasibility, a PI dosage of 0.8 g L^{-1} was identified as the most suitable operating condition for CBF degradation in the SA/WLBC/HGMs–PI/light system.

3.2.6. Pollutant concentration. The influence of the initial CBF concentration (15–35 mg L^{-1}) on its removal performance in the SA/WLBC/HGMs–PI/light system was investigated under the following conditions: a catalyst dosage of 4 g, a PI concentration of 0.8 g L^{-1}, an input flow rate of 2 mL min^{-1}, neutral pH, and ambient temperature, as shown in Fig. 4f. After 300 min of reaction, the CBF removal efficiencies reached 94.25, 88.29, 80.65, 67.37, and 61.12% for initial CBF concentrations of 15, 20, 25, 30, and 35 mg L^{-1}, respectively. The corresponding pseudo-first-order kinetic rate constants were 0.0113, 0.0087, 0.0066, 0.0046, and 0.0038 min^{-1}. A clear decline in degradation efficiency was observed as the initial CBF concentration increased. This behavior can be attributed primarily to the saturation of available adsorption and catalytically active sites on the beads at higher pollutant loadings, which restricts effective contact between CBF molecules and reactive species. In addition, elevated CBF concentrations promote the formation and accumulation of intermediate degradation products, which compete further with the parent CBF molecules for the limited active sites and ROS generated from PI activation. Consequently, intensified molecular competition and insufficient availability of reactive species jointly contribute to reduced removal efficiency at higher concentrations.[83,84] These results indicate that the SA/WLBC/HGMs–PI/light system exhibits superior degradation performance at relatively low CBF concentration, highlighting its suitability for treating water contaminated with low to moderate pesticide levels. Considering the environmentally relevant concentrations of CBF typically encountered in real water matrices, an initial CBF concentration of 15 mg L^{-1} was therefore selected as the representative condition for subsequent experiments aimed at evaluating the system performance under varying environmental conditions.

3.2.7. Reaction time. The influence of reaction time on CBF degradation was evaluated under various operating conditions, as illustrated in all the parameter-dependent figures (Fig. 4a–f). In all cases, CBF removal efficiency increased rapidly during the initial reaction period, consistent with pseudo-first-order kinetics, where a high concentration of active oxidizing species and abundant available reaction sites promote fast degradation. After approximately 200 min, the reaction rate decreased markedly, and the removal efficiency approached a steady state, with only a minor further increase observed at longer reaction times. This kinetic slowdown can be attributed to the progressive depletion of readily available CBF molecules, which reduces the driving force of the degradation reaction, as well as to the consumption of ROS and partial saturation or deactivation of active sites on the catalyst surface. Additionally, mass transfer limitations and the establishment of a near-equilibrium state between degradation and intermediate accumulation may further restrict reaction progress at prolonged times.[85,86] Therefore, a reaction duration of 200 min was selected for subsequent experiments, as it is sufficient to achieve near-maximum CBF removal while ensuring efficient operation and avoiding unnecessary energy and time consumption.

3.3. Mechanistic study of the oxidation process

3.3.1. Identification of dominant oxidizing species. In our system, the biochar beads can act as activators of PI in addition to PI activation induced by light irradiation. However, when PI is absent, irradiation of the biochar beads alone cannot achieve effective degradation due to the modest photocatalytic properties of pristine biochar catalysts.[12,18] To support our claim, the degradation of CBF in the continuous-flow reactor was performed in the presence of light and biochar beads without PI. The degradation efficiency decreased sharply to only 6% compared to 94.11% in the presence of PI, confirming that the degradation was due mainly to PI activation by light and functional groups, not photocatalysis. Previous studies have demonstrated that a variety of reactive species, including $IO_4^{\bullet}$, $IO_3^{\bullet}$, $^{\bullet}OH$, $O_2^{\bullet-}$, $^1O_2$, and $O(^3P)$, are commonly generated in PI-based systems and play critical roles in pollutant degradation.[41,87] To elucidate the relative contributions of these reactive

species to CBF degradation in the SA/WLBC/HGMs–PI/light system, a series of radical quenching experiments was conducted under the optimum operating conditions. Before initiating the reaction, specific scavengers (15 mM) were introduced into the influent CBF solution. As illustrated in Fig. 5, the CBF removal efficiency decreased from 94.11% (first-order rate K_{obs} = 0.0124 min^{-1}) in the absence of quenchers to 9.04% (first-order K_{obs} = 0.0005 min^{-1}), 77.62% (first-order K_{obs} = 0.0074 min^{-1}), and 67.63% (first-order K_{obs} = 0.0057 min^{-1}) in the presence of furfuryl alcohol, chloroform, and tert-butanol, respectively. The addition of 15 mM phenol markedly reduced the CBF removal efficiency to 16.62%, accompanied by a substantial decrease in first-order K_{obs} to 0.0011 min^{-1}. Conversely, KI significantly inhibited CBF degradation, reducing the removal efficiency to 29.93% with a corresponding pseudo-first-order rate constant of 0.0019 min^{-1}. In addition, the presence of 2-propanol suppressed CBF degradation, reducing the removal efficiency to 65% with a first-order rate constant of 0.0054 min^{-1}. The results of radical quenching experiments clearly demonstrate that CBF degradation in the SA/WLBC/HGMs–PI/light system is governed by multiple ROS, each making a distinct contribution. The dramatic inhibition observed upon furfuryl alcohol introduction identifies $^1O_2$ as the dominant oxidizing species, indicating that CBF degradation proceeds primarily *via* a non-radical pathway. In contrast, the moderate suppression caused by chloroform and *tert*-butyl alcohol confirms the involvement of $O_2^{\bullet-}$ and $^{\bullet}OH$, respectively, although their contributions are comparatively minor. Moreover, the addition of 2-propanol resulted in only a marginal further decrease in CBF degradation efficiency (~1.6%) compared to *tert*-butyl alcohol, indicating that $O(^3P)$ contributes negligibly to the overall degradation process. Notably, the pronounced decrease in the degradation efficiency in the presence of phenol and KI highlights the significant synergistic role of $IO_4^{\bullet}$ and $IO_3^{\bullet}$ in the CBF degradation process. Based on the degree of inhibition observed in the scavenging experiments, the relative contributions of reactive species to CBF degradation in the SA/WLBC/HGMs–PI/light system can be ranked as follows: $O(^3P) < O_2^{\bullet-} < {}^{\bullet}OH < IO_4^{\bullet}/IO_3^{\bullet} < {}^1O_2$. Numerous studies on PI-based AOPs have consistently identified $^1O_2$ as the dominant reactive species responsible for the degradation of organic pollutants.[20,73,88,89]

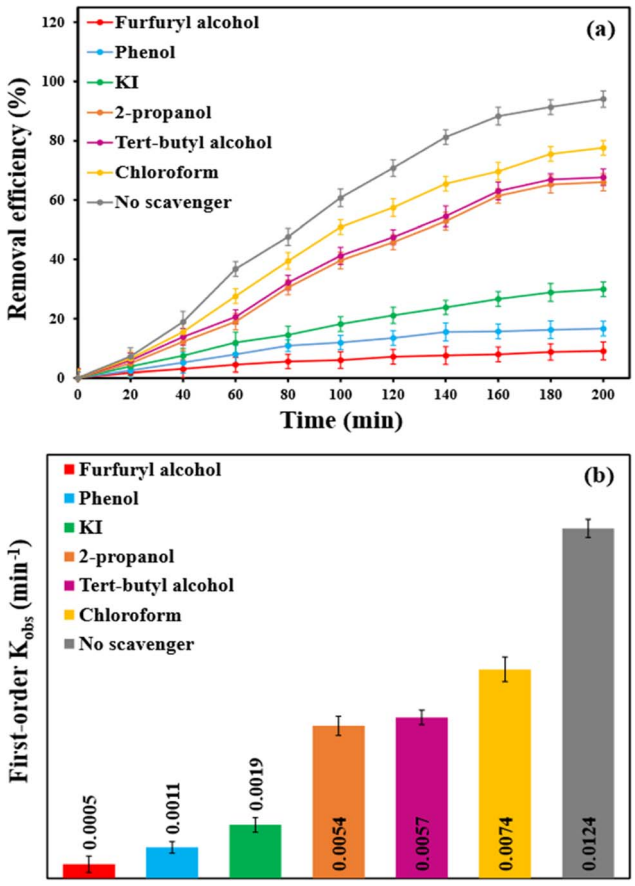

Fig. 5 Effect of reactive species scavengers (15 mM) on CBF degradation in the SA/WLBC/HGMs–PI/light system under the optimum conditions: (a) CBF removal efficiency and (b) corresponding pseudo-first-order K_{obs} values.

3.3.2. Plausible degradation mechanism for CBF. Based on the radical quenching experiments and the observed contribution order of reactive species, a comprehensive mechanistic pathway for CBF degradation in the SA/WLBC/HGMs–PI/light system is proposed, as presented in Fig. 6. Upon light irradiation, IO_4^- may undergo photolytic cleavage to generate different ROS through multiple parallel pathways. As described in Table S7, eqn (1) and (2), photoexcited IO_4^- may yield $IO_3^{\bullet}$ and $O^{\bullet-}$, as well as $O(^3P)$. The $O(^3P)$ generated can subsequently react with dissolved oxygen to form ozone (Table S7, eqn (3)), which subsequently oxidizes $IO_3^{\bullet}$ back to $IO_4^{\bullet}$ while regenerating O_2 (Table S7, eqn (4)), thereby sustaining the iodine redox cycle. Meanwhile, $O^{\bullet-}$ can be protonated or hydrolyzed to produce $^{\bullet}OH$ (Table S7, eqn (5) and (6)).[42,90] In addition to photolysis, surface oxygen-containing functional groups may also contribute significantly to ROS formation. As shown in Table S7, eqn (7) and (8), surface oxygen-containing functional groups can interact with IO_4^- to form surface oxygen-centered radicals, releasing $^{\bullet}OH$ and $IO_3^{\bullet}$.[20,91] The iodine radicals may further participate in interconversion reactions with IO_4^- (Table S7, eqn (9)) and can be regenerated through reactions with $^{\bullet}OH$ (Table S7, eqn (16) and (17)), reinforcing the iodine-centered radical pool.[42] Moreover, IO_4^- may react with hydroxide ions and dissolved oxygen to produce $O_2^{\bullet-}$ (Table S7, eqn (12) and (13)), further enriching the ROS network.[42] The singlet oxygen, identified as the dominant oxidizing species in the scavenger experiments, can be produced through multiple converging pathways. As illustrated in Table S7, eqn (14), the recombination of $IO_4^{\bullet}$ radicals may directly yield $^1O_2$, while reactions involving $O_2^{\bullet-}$, IO_4^-, and water can also contribute to the formation of $^1O_2$ (Table S7, eqn (15)). Additional $^1O_2$ may be generated through the reaction of $O_2^{\bullet-}$ with $^{\bullet}OH$ (Table S7, eqn (16)) or water (Table S7, Eq (17)); the latter may simultaneously lead to the formation of H_2O_2. The generated H_2O_2 can further participate in ROS interconversion; it may react with $O_2^{\bullet-}$ to generate additional $^{\bullet}OH$ and $^1O_2$ (Table S7, eqn (18)) and can also interact with IO_4^- to produce $O_2^{\bullet-}$ and $IO_3^{\bullet}$ radicals (Table S7, eqn (19)).[42,90,91] Subsequently, the generated ROS may attack

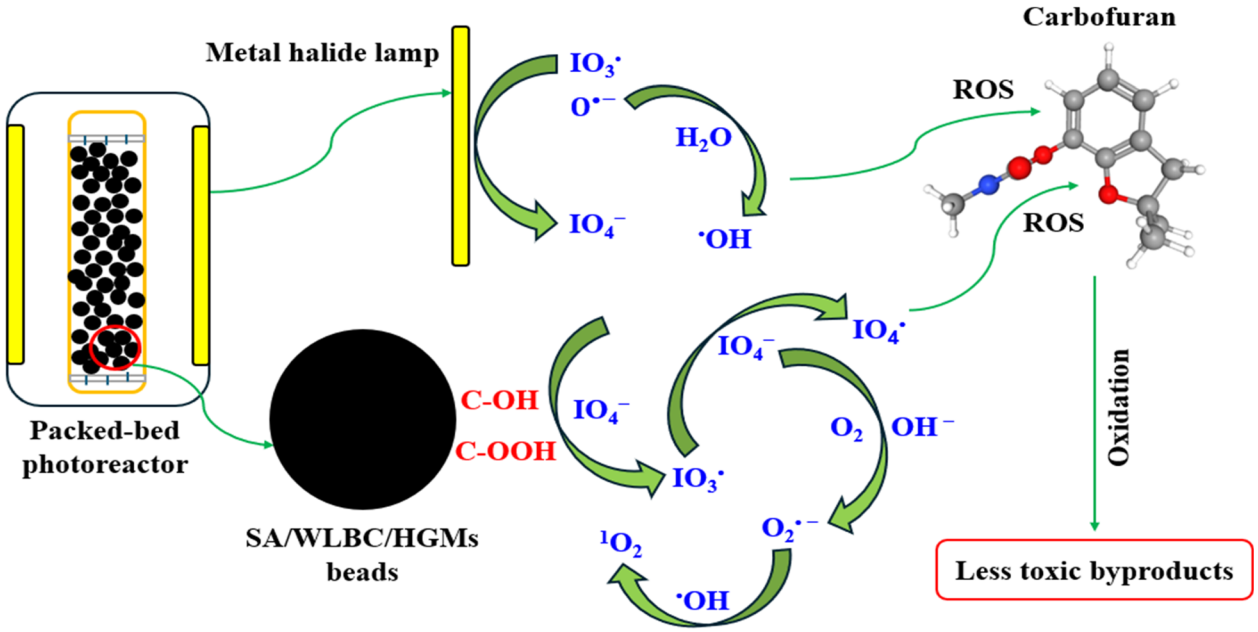

Fig. 6 Schematic illustration of the plausible CBF degradation mechanism in the SA/WLBC/HGMs–PI/light process.

and oxidize CBF molecules, leading to their transformation into various intermediate products, which can undergo further oxidative degradation and mineralization to ultimately yield carbon dioxide and water.

3.4. Environmental footprint of the SA/WLBC/HGMs–PI/light system

3.4.1. Generation and transformation of iodine species. The potential formation of toxic iodinated byproducts represents one of the major concerns and practical limitations associated with the application of PI-based AOPs in water treatment.[92,93] Accordingly, the transformation pathways of PI during CBF oxidation in the SA/WLBC/HGMs–PI/light system were systematically investigated by monitoring all relevant iodine species, including IO_4^-, IO_3^-, I^-, I_2, I_3^-, and HOI, under optimal operating conditions. As shown in Fig. 7a, the progressive degradation of CBF was accompanied by continuous consumption of IO_4^-, which was gradually and completely converted to IO_3^-. The steady accumulation of IO_3^-, recognized as a stable and environmentally benign iodine sink, indicates a favorable transformation pathway for iodine species.[94] Additionally, potentially hazardous reactive iodine species, such as I^-, I_2, I_3^-, and HOI, were not detected throughout the reaction. These results demonstrate that the SA/WLBC/HGMs–PI/light system enables efficient contaminant removal while effectively suppressing the formation of toxic iodinated byproducts, thereby underscoring the sustainability and operational safety of the proposed PI-based system. This characteristic is particularly advantageous for its application in rapid or emergency water purification scenarios, where both treatment efficiency and public health protection are critical.

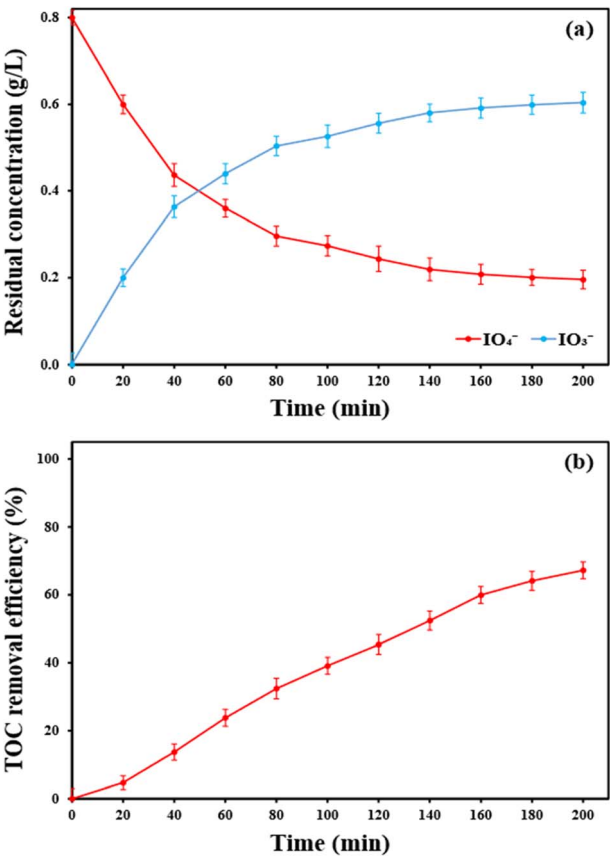

Fig. 7 (a) TOC mineralization efficiency of CBF and (b) transformation profiles of iodine species during CBF oxidation in the SA/WLBC/HGMs–PI/light system under the optimal operating conditions.

Moreover, a substantial depletion of IO_4^- (75.51%) was achieved after 300 min of reaction, further highlighting the high efficiency of the SA/WLBC/HGMs–PI/light system in activating and utilizing PI. This indicates that the oxidant was effectively involved in the oxidation process rather than remaining unreacted in solution, reflecting efficient electron transfer and catalytic activation under the applied operating conditions. The high degree of PI utilization also suggests minimized wastage of oxidant, which is advantageous from both economic and environmental perspectives.

3.4.2. Identification of degradation byproducts and toxicity assessment. To elucidate the formation and transformation of CBF degradation intermediates in the SA/WLBC/HGMs–PI/light system, the mineralization performance was systematically evaluated over time by monitoring total organic carbon (TOC). As illustrated in Fig. 7b, TOC removal increased progressively throughout the reaction, reaching 67.21% after 200 min. This result demonstrates that, although a significant fraction of CBF was mineralized to inorganic end products (CO_2 and H_2O), complete mineralization was not achieved within the investigated period. Instead, a considerable portion of CBF was transformed into intermediate organic species, indicating a stepwise degradation mechanism. The degradation process involved multiple oxidative transformations of functional groups, including oxidation, hydroxylation, and bond cleavage. These sequential reactions are typically induced by ROS generated in the SA/WLBC/HGMs–PI/light system, which progressively destabilize the molecular structure of CBF and promote its breakdown into smaller and more oxidized fragments. Liquid chromatography–mass spectrometry (LC-MS) analysis (Fig. S7) enabled the identification of several intermediate products, suggesting a plausible degradation pathway (Fig. 8). The parent compound, CBF (*m*/*z* 222), underwent hydroxylation to produce 4,5-dihydroxy-2,2-dimethyl-2,3-dihydrobenzofuran-7-yl methylcarbamate (P1, *m*/*z* 254). In a parallel pathway, CBF can also undergo bond cleavage to form carbofuran phenol (2,2-dimethyl-2,3-dihydrobenzofuran-7-ol) at *m*/*z* 165, denoted P2, as previously reported.[95] Subsequently, P2 is further oxidized by the generated reactive species, forming 3-(2-hydroxy-2-methylpropyl)benzene-1,2-diol (P3, *m*/*z* 183) and 3-(2-hydroxy-2-methylpropyl)benzene-1,2,4-triol (P4, *m*/*z* 199).[96] Through continuous ROS-mediated degradation, the smaller organic molecules were progressively oxidized and ultimately converted into CO_2 and H_2O.

To evaluate the ecological risks associated with CBF degradation, the acute toxicity of CBF and its identified intermediates were predicted. Acute toxicity was assessed in terms of the half-lethal concentration (LC_{50}) toward *Daphnia magna* (48 h exposure) and fathead minnow (96 h exposure). In this context, higher LC_{50} values correspond to lower toxicity. As shown in Fig. 9a, the predicted 96 h LC_{50} values for fathead minnow increased for most degradation intermediates (P2, P3, and P4) compared with the parent compound, indicating reduced toxicity following transformation. However, intermediate P1 exhibited a lower LC_{50} value than CBF, suggesting slightly higher toxicity toward the fathead minnow. In the case of *Daphnia magna*, all identified intermediates displayed higher LC_{50} values than CBF, reflecting a general decline in acute toxicity after degradation (Fig. 9b). Among the intermediates, P3 showed the highest LC_{50} value, indicating the lowest predicted toxicity, whereas P1 exhibited only a marginal change relative to the parent compound.

Overall, the predicted toxicity trends demonstrate that the degradation process in the studied system transforms CBF structurally and reduces its ecological hazard in most cases. This decline in acute toxicity highlights the environmental relevance and practical potential of the developed degradation

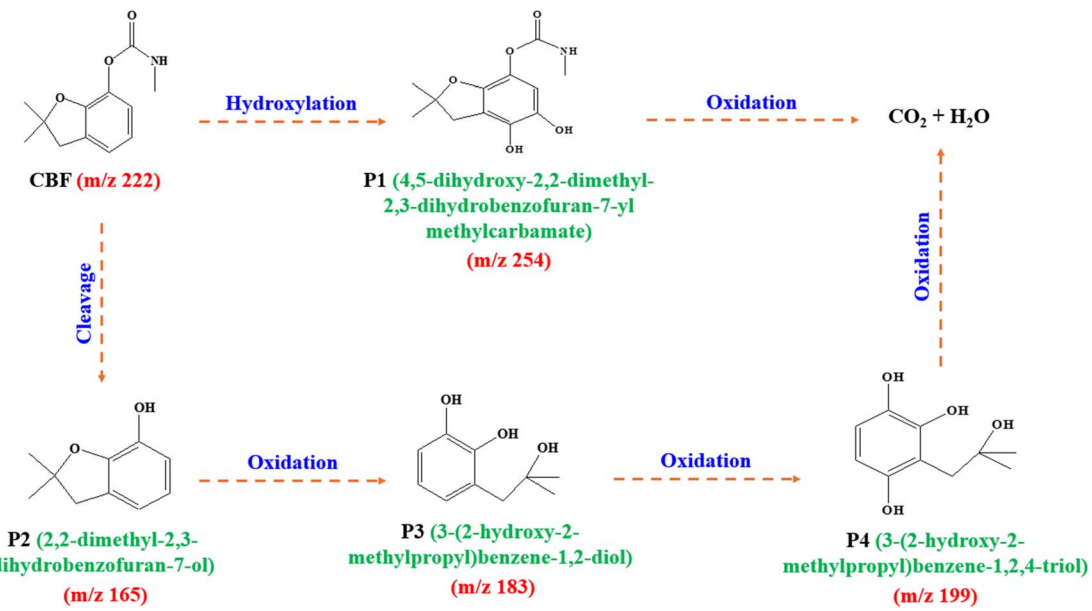

Fig. 8 Proposed degradation pathway of CBF in the SA/WLBC/HGMs–PI/light system.

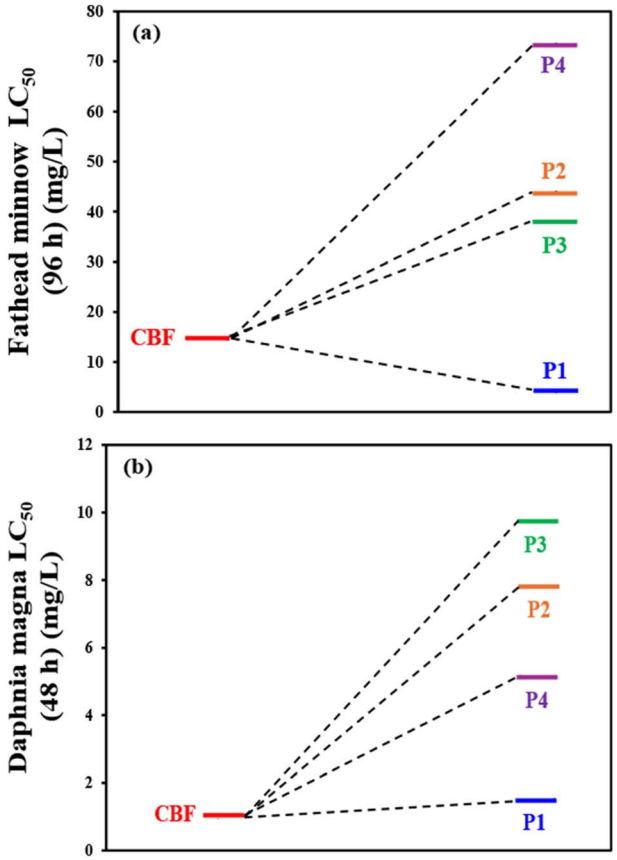

Fig. 9 Toxicity of CBF and its byproducts towards (a) fathead minnow LC_{50} and (b) *Daphnia magna* LC_{50}.

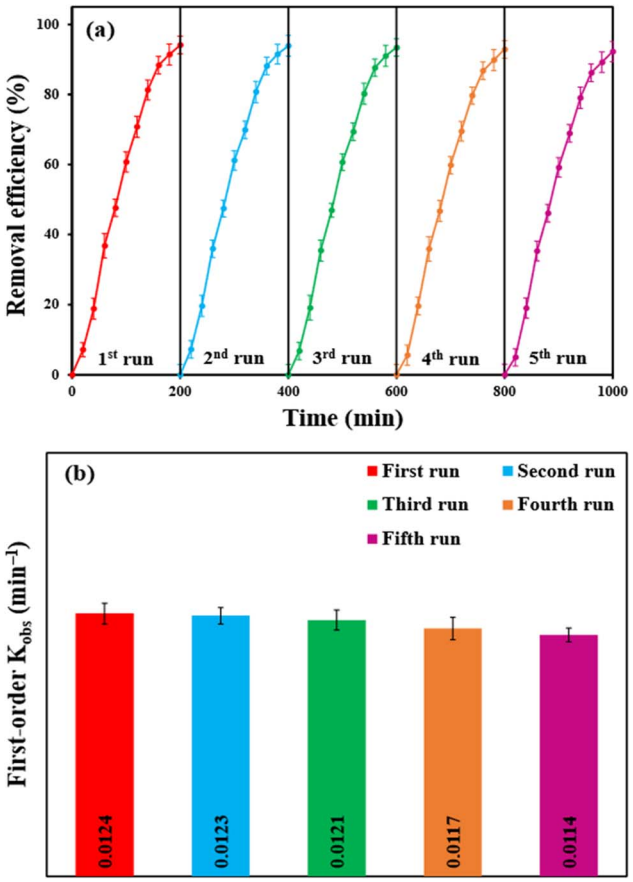

Fig. 10 Reusability of the SA/WLBC/HGMs–PI/light system for CBF removal under the optimum conditions: (a) CBF degradation efficiency over five consecutive runs and (b) resulting first-order kinetic analysis.

system for mitigating CBF-related risks in aquatic environments.

3.5. Practical applicability of the SA/WLBC/HGMs–PI/light system

3.5.1. Recycling performance of the SA/WLBC/HGMs beads. The recyclability of the SA/WLBC/HGMs beads was investigated over five consecutive degradation cycles conducted under the previously optimized reaction conditions. As presented in Fig. 10a, the CBF removal efficiency in the SA/WLBC/HGMs–PI/light system exhibited only a slight decline, decreasing from 94.11% in the first run to 93.89%, 93.39%, 92.87%, and 92.25% in the second, third, fourth, and fifth cycles, respectively. A corresponding gradual decline in the apparent pseudo-first-order rate constant was observed, decreasing from 0.0124 min^{-1} to 0.0123, 0.0121, 0.0117, and 0.0114 min^{-1} over repeated use (Fig. 10b). Compared with other recently reported alginate-based catalytic systems, the SA/WLBC/HGMs beads demonstrate superior stability. Magnetic biochar-iron-lanthanum crosslinked alginate beads exhibited an approximately 10.65% decrease in tetracycline hydrochloride removal efficiency after six successive cycles when employed as a catalyst in a peroxymonosulfate oxidation system.[71] Zouggari *et al.* reported a 9.3% decrease in sulfamethoxazole degradation efficiency after six consecutive cycles during its photocatalytic degradation *via* visible-light-assisted peroxymonosulfate activation.[97] In contrast, the substantially lower reduction in CBF removal efficiency (1.86%) observed over five consecutive cycles in the SA/WLBC/HGMs–PI/light system in the present study highlights the excellent reusability of the SA/WLBC/HGMs beads and confirms their potential suitability for long-term water treatment applications. This outstanding stability can be attributed to the strong immobilization of active species within the alginate matrix and the incorporation of HGMs, which enhance the mechanical robustness and structural integrity of the beads during repeated handling and agitation.[36,38,55] However, the progressive decline in degradation efficiency during successive cycles can be attributed to partial deactivation of active sites resulting from the deposition of intermediate byproducts formed during CBF oxidation. Their accumulation on the bead surface restricts the diffusion of reactants and ROS, limiting access to active sites.[64,98]

3.5.2. Effect of inorganic anions and natural organic matter. The widespread presence of inorganic anions and NOM in real water bodies can markedly influence the performance of AOPs.[39] To assess the robustness of the SA/WLBC/HGMs–PI/light system under realistic conditions, the degradation of CBF was evaluated in the presence of several common inorganic anions (HCO_3^-, NO_3^-, SO_4^{2-}, Cl^-, and HPO_4^{2-}), each at an

initial concentration of 15 mM. The corresponding results are presented in Fig. 11a. Among the investigated anions, HCO_3^- exerted the most pronounced inhibitory effect on CBF degradation. Under the optimum conditions, the CBF removal efficiency decreased to 80.58%, with a pseudo-first-order rate constant of 0.0078 min^{-1}, compared to 94.11% and 0.0124 min^{-1} in the absence of added anions. In contrast, NO_3^-, SO_4^{2-}, Cl^-, and HPO_4^{2-} caused relatively minor suppression effects, yielding CBF removal efficiencies of 87.18, 88.34, 90.89, and 91.45%, and corresponding first-order K_{obs} values of 0.0096, 0.0099, 0.0109, and 0.0112 min^{-1}, respectively. Accordingly, the inhibitory influence of the tested anions followed the order: $HCO_3^- > NO_3^- > SO_4^{2-} > Cl^- > HPO_4^{2-}$. The observed decline in CBF removal efficiency in the presence of inorganic anions can be attributed to several concurrent mechanisms. Anions may competitively adsorb onto the surface of the SA/WLBC/HGMs beads *via* non-covalent interactions, thereby occupying active sites and hindering CBF adsorption. In addition, the accumulation of inorganic anions on the catalyst surface may form a passivating inorganic layer that partially blocks reactive sites and impedes mass transfer of both oxidants and target pollutants.[88,99] Furthermore, these anions can scavenge ROS, converting them into less reactive intermediates and consequently reducing the overall oxidation capacity of the system.[84,100] In some cases, anion-induced agglomeration on the biochar surface may further decrease the availability of effective binding sites, leading to diminished degradation efficiency.[20,101] Notably, HCO_3^- exhibited the strongest inhibitory effect, which can be attributed to its role as a radical scavenger. HCO_3^- may also undergo complexation reactions with catalytic components, resulting in the formation of aqueous complexes or precipitates that suppress ROS generation and further hinder CBF degradation.[88,99]

Similarly, the presence of HA, a representative NOM constituent, significantly affected the degradation performance of CBF, as depicted in Fig. 11b. When HA was introduced at concentrations of 2, 5, and 10 mg L^{-1}, the CBF removal efficiencies declined to 89.74%, 84.73%, and 83.21%, respectively, with corresponding pseudo-first-order rate constants of 0.0106, 0.0090, and 0.0084 min^{-1}. These results demonstrate a pronounced reduction in CBF degradation efficiency as the HA concentration increased to 5 mg L^{-1}, whereas further increases in HA concentration caused only slight additional changes. The inhibitory effect of HA can be attributed primarily to its rich abundance of hydroxyl and carboxyl functional groups, which facilitate its adsorption onto the catalyst surface.[102,103] This adsorption can block reactive sites, suppress pollutant uptake, and hinder effective contact between oxidants and catalytic active sites. In addition, HA may compete directly with CBF for reactive oxidative species within the system, further limiting the availability of these species for CBF degradation.[104] Despite the inhibitory influence of coexisting inorganic anions and organic matter, the SA/WLBC/HGMs–PI/light system maintained high catalytic performance, indicating strong tolerance, operational stability, and selective oxidation

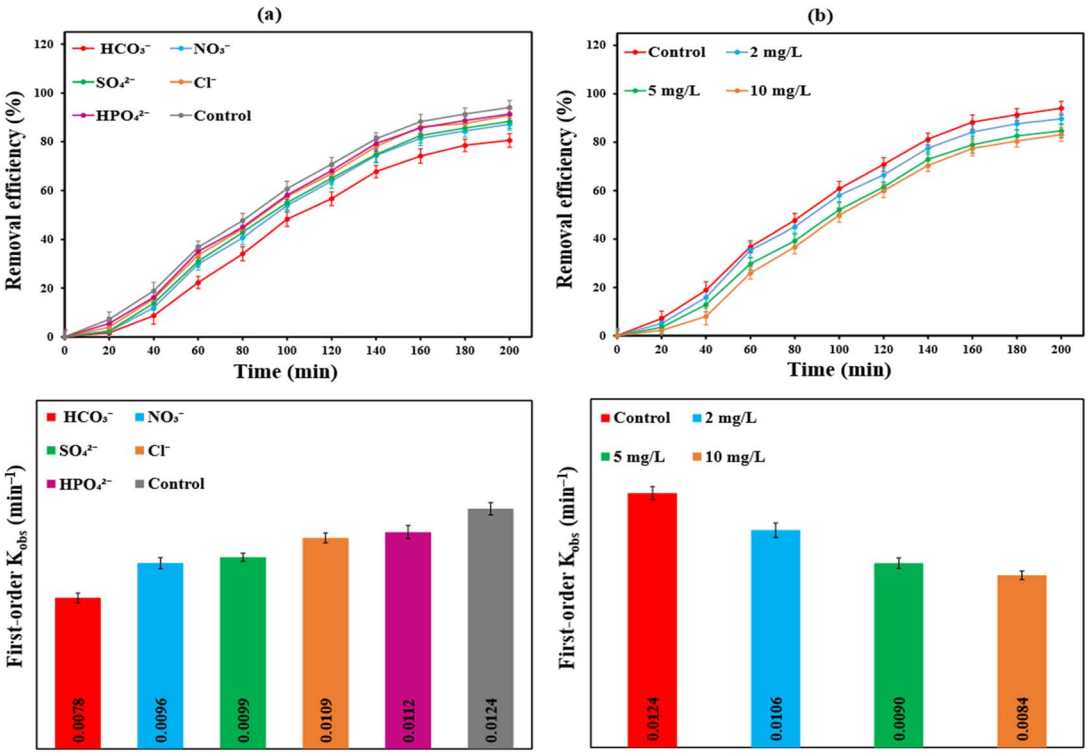

Fig. 11 Effect of common coexisting substances on CBF removal in the SA/WLBC/HGMs–PI/light system: (a) influence of inorganic anions and (b) humic acid. Conditions: $[catalyst]_o = 4$ g, $[PI]_o = 0.8$ g L^{-1}, input flow rate = 2 mL min^{-1}, pH = 7, $T = 25$ °C, $[CBF]_o = 15$ mg L^{-1}, and $[inorganic\ anion]_o = 10$ mM.

ability for the efficient removal of organic micropollutants under realistic water matrix conditions.

3.5.3. Performance validation in actual water matrices. Real water matrices are typically rich in inorganic ions and dissolved organic matter, which can impede catalytic degradation processes.[99,100] Therefore, the practical applicability of the SA/WLBC/HGMs–PI/light system was assessed by examining CBF degradation in a range of real water matrices, including tap water, river water collected from the Nile River (Cairo, Egypt), seawater obtained from the Mediterranean Sea (Alexandria, Egypt), and lake water sampled from Lake Mariout (Alexandria, Egypt). The collected water matrices were allowed to stand undisturbed for 24 h to facilitate sedimentation of suspended solids. The supernatants were then carefully separated and used individually for the preparation of the pollutant solutions. Their fundamental physicochemical characteristics are summarized in Table S8. Under the optimized conditions, the CBF removal efficiency after 200 min decreased from 94.11% in deionized water to 91.24%, 89.99%, 86.06%, and 83.06% in tap water, river water, seawater, and lake water, respectively (Fig. 12a). The corresponding pseudo-first-order rate constants were 0.0111, 0.0105, 0.0095, and 0.0087 min^{-1}, compared with 0.0124 min^{-1} in deionized water (Fig. 12b). The comparatively high removal efficiencies achieved in deionized and tap water demonstrate that low levels of DOM and inorganic ions exert a negligible impact on the catalytic performance of the system. In contrast, a modest decline in removal efficiency was observed in river, lake, and seawater matrices, which can be attributed primarily to their higher contents of DOM and inorganic ions. These constituents may competitively adsorb onto the catalyst surface, thereby blocking active sites, or act as scavengers for ROS, reducing their availability for the degradation of target pollutants.[105,106] Furthermore, the elevated turbidity and high concentrations of dissolved solids in these water matrices can scatter or attenuate incident light, hindering the efficient photoactivation of PI and consequently diminishing overall degradation efficiency.[107] Overall, these results confirm that the BFC-beads/PMS system maintains robust catalytic performance and strong environmental adaptability in complex real water matrices.

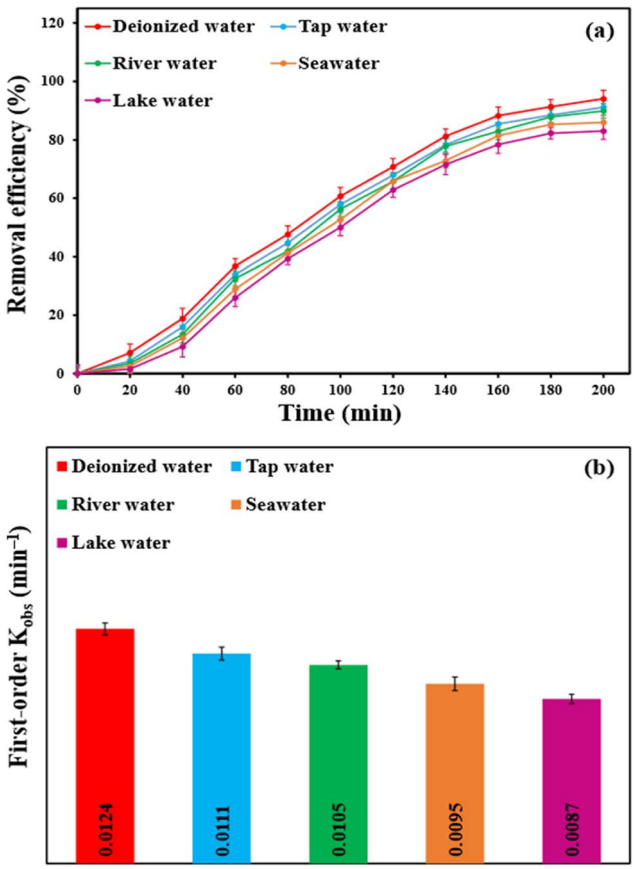

Fig. 12 Effect of different water matrices on the catalytic performance of the SA/WLBC/HGMs–PI/light system under the optimum conditions: (a) CBF removal efficiency and (b) corresponding pseudo-first-order kinetic behavior assessment.

3.5.4. Effect of different pesticides. To further assess the versatility of the SA/WLBC/HGMs–PI/light system, additional pesticides apart from CBF were selected as target contaminants, including diazinon, malathion, and chlorpyrifos. All experiments were conducted under identical operating conditions: catalyst dosage of 4 g, initial PI concentration of 0.8 g L^{-1}, influent flow rate of 2 mL min^{-1}, initial pH of 7, reaction temperature of 25 °C, and initial pollutant concentration of 15 mg L^{-1}. As shown in Fig. 13a, the pollutant removal efficiencies and corresponding apparent first-order rate constants followed the order: CBF (94.11%, first-order K_{obs} = 0.0124 min^{-1}) > diazinon (89.77%, first-order K_{obs} = 0.0111 min^{-1}) > malathion (84.50%, first-order K_{obs} = 0.0098 min^{-1}) > chlorpyrifos (78.12%, first-order K_{obs} = 0.0077 min^{-1}). TOC measurements confirmed that the investigated pesticides underwent partial mineralization. The TOC removal efficiencies reached 64.32% for diazinon, 58.94% for malathion, and 51.85% for chlorpyrifos, whereas CBF exhibited a higher mineralization efficiency of 67.21% (Fig. 13a). These results indicate varying extents of organic carbon conversion among the tested compounds. The lower mineralization efficiency relative to the individual pollutant removal percentages suggests that a fraction of the degraded parent compounds was converted into intermediate transformation products rather than being fully oxidized to CO_2 and H_2O. Some of these intermediates are likely to be more recalcitrant and resistant to further oxidative attack, limiting complete mineralization within the tested reaction time.[94] The observed variation in the system performance can be attributed to differences in molecular structure, electron density distribution, steric effects, and adsorption affinity toward the biochar matrix, all of which influence susceptibility to ROS generated during PI activation under light irradiation.[84,94] Overall, the consistently high removal efficiencies across structurally diverse compounds demonstrate the strong oxidative capacity and functional adaptability of the SA/WLBC/HGMs–PI/light system, underscoring its significant potential for practical water treatment applications involving various classes of organic micropollutants. Nevertheless, the detailed degradation pathways and dominant ROS responsible for the transformation of each

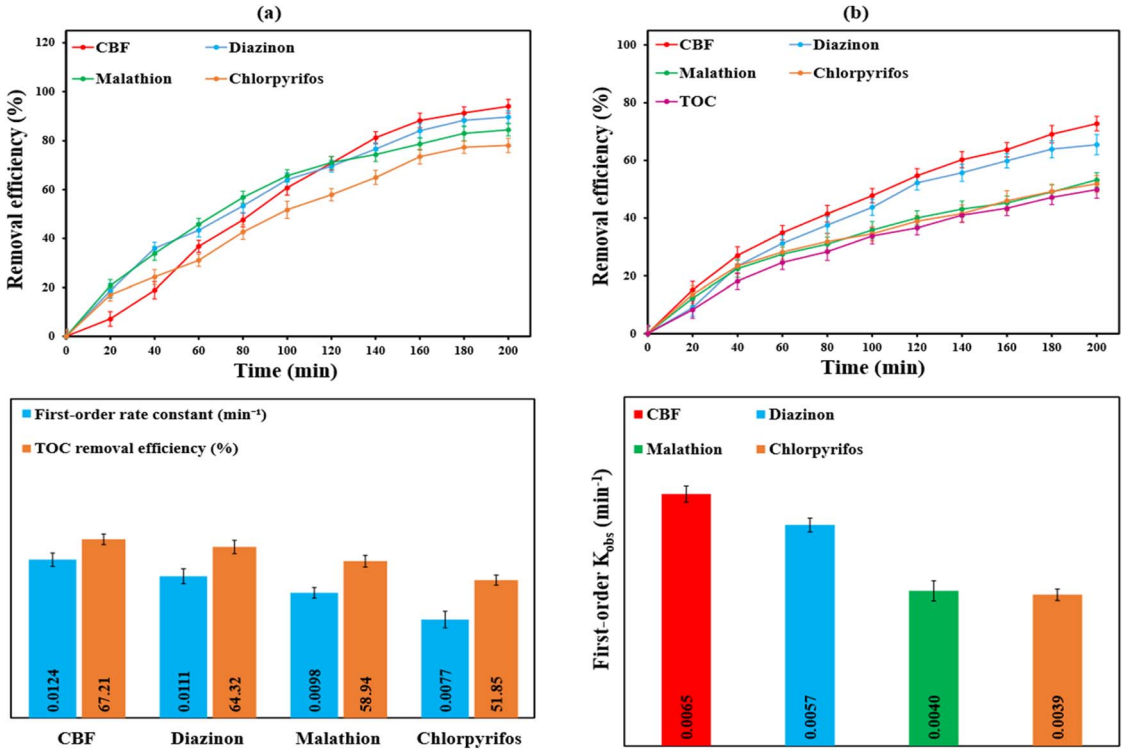

Fig. 13 Treatment performance of the SA/WLBC/HGMs–PI/light system for: (a) individual pesticide solutions and (b) mixed-pesticide wastewater. Conditions: $[catalyst]_o = 4$ g, $[PI]_o = 0.8$ g L^{-1}, input flow rate = 2 mL min^{-1}, pH = 7, $T = 25$ °C, $[single\ pesticide]_o = 15$ mg L^{-1}, and initial TOC of the mixed-pesticide wastewater = 27.38 mg L^{-1}.

pesticide warrant further mechanistic investigation to fully elucidate the underlying reaction mechanisms.

Moreover, considering that multiple contaminants typically coexist in real aquatic environments, the performance of the SA/WLBC/HGMs–PI/light system was further evaluated using a mixed pesticide solution containing CBF, diazinon, malathion, and chlorpyrifos, each at an initial concentration of 15 mg L^{-1}. The experiments were performed under the same operating conditions as in the single-pesticide tests (catalyst dosage = 4 g, PI concentration = 0.8 g L^{-1}, influent flow rate = 2 mL min^{-1}, initial pH = 7, and reaction temperature = 25 °C) to ensure direct comparability with the single-pollutant experiments. As illustrated in Fig. 13b, the removal efficiencies for CBF, diazinon, malathion, and chlorpyrifos in the mixed system reached 72.78%, 65.49%, 53.25%, and 51.88%, respectively, while the corresponding first-order rate constants were 0.0065, 0.0057, 0.004, and 0.0039 min^{-1}. The degradation efficiencies and kinetic rates were slightly lower than those obtained in the single-contaminant experiments. This modest decline in performance can be attributed to competitive interactions among coexisting pollutants. In a multi-component system, different pesticide molecules compete for active sites on the catalyst surface and for ROS generated during PI activation under light irradiation. Additionally, intermediate products formed from one compound may scavenge ROS or occupy adsorption sites, partially inhibiting the degradation of other coexisting contaminants. As natural waters contain mixtures of micropollutants at trace (μg L^{-1}) levels,[108] the ability of the SA/WLBC/HGMs–PI/light system to simultaneously degrade structurally diverse pesticides at higher concentrations demonstrates its strong potential for practical wastewater treatment applications, enabling the one-step removal of complex contaminant mixtures rather than single-compound elimination. Furthermore, the TOC removal efficiency of 49.87% (Fig. 13b), calculated for the overall mixed solution with an initial TOC of 27.38 mg L^{-1}, underscores the practical significance of the SA/WLBC/HGMs–PI/light system beyond the mere degradation of the parent compounds. In real wastewater treatment applications, partial mineralization is particularly important because it reduces the overall organic load, toxicity, and oxygen demand of the effluent before discharge or subsequent biological polishing.[77] Although complete mineralization was not attained within the tested reaction time, the substantial TOC reduction indicates effective breakdown of complex pesticide structures into smaller, more biodegradable intermediates. This suggests that the proposed system can serve as an efficient pre-treatment step in integrated treatment trains, enhancing the overall removal efficiency and improving the compatibility of treated effluents with downstream biological or physicochemical processes.

3.5.5. Techno-economic feasibility evaluation of the degradation system. The feasibility of the SA/WLBC/HGMs–PI/light degradation system for the degradation of mixed-pesticide wastewater was evaluated by estimating the capital cost, operating cost, revenue, and profit. Sensitivity analysis was further conducted to evaluate the economic stability of the

system towards price variations. The details of cost parameters are scheduled in Table S9. The total capital expenditure (CAPEX) included the cost of the reactor, associated equipment (*e.g.*, hotplate stirrer and pumps), as well as expenses allocated for emergency cases. The reactor cost was estimated based on a total volume of 10 m^3 and construction from reinforced concrete. The treatment cycle time was assumed to be 4 h, with 8 operating hours per day, resulting in two cycles per day. Accordingly, the system was designed to treat 20 m^3 day^{-1}, corresponding to 6000 m^3 $year^{-1}$ over 300 working days per year. The reactor lifetime was assumed to be 10 years. Furthermore, the total reactor cost included expenditures related to contracting, engineering design, as well as electrical and plumbing installations, in accordance with the approach reported by Emmanuel *et al.*[109] The cost of equipment was estimated based on purchasing two pumps, three hotplate stirrers, an oven, a muffle furnace, a centrifuge, and an electric blender, where one pump and two stirrers can be in service, and the others can be spares. The unit capital cost was estimated to be 0.8 USD/m^3.

The operational expenditure (OPEX) comprised the costs of chemicals, energy consumption, labor, taxes, and maintenance. The chemical cost was calculated based on the applied dosages and corresponding market prices, as detailed in Table S9. The energy cost was estimated according to the power requirements of the equipment during operation. In addition, labor, taxes, and maintenance expenses were approximated as a percentage of the annual capital cost. Based on these estimations, the unit operating cost was determined to be 1.14 USD/m^3.

With respect to revenue generation, the reclaimed water can be commercialized for non-potable applications, such as car washing.[110,111] In addition, the fabricated beads may be marketed to industrial facilities for use in the treatment of contaminated effluents. Moreover, the reduction in TOC can represent an additional revenue stream when monetized based on an assigned shadow price, as detailed in Table S9.

The profitability indicators of the techno-economic assessment for the SA/WLBC/HGMs–PI/light degradation system were evaluated to determine its financial feasibility. The results revealed a payback period of 5.5 years, a positive net present value (NPV), an internal rate of return (IRR) exceeding the prevailing discount rate, and a profitability index greater than 1. Collectively, these indicators confirm the economic viability of the proposed system and highlight its potential attractiveness for stakeholder investment. To further evaluate the economic robustness of the project, the NPV was assessed by varying key parameters, including chemical cost, capital cost, reclaimed water price, and bead price, by ±20% (Fig. 14). The findings indicate that the proposed system maintains overall economic stability under these fluctuations. However, variations in the bead price show a pronounced influence on project feasibility, highlighting its critical role in the economic performance of the system.

The total treatment cost of the proposed system (1.94 USD/m^3) was compared with those reported in previous studies to further assess the economic feasibility of the system. Dadebo *et al.* reported a total cost of 1.54 USD/m^3 for an anaerobic digestion/phytoremediation/co-pyrolysis system applied to industrial wastewater treatment.[112] Emmanuel *et al.*

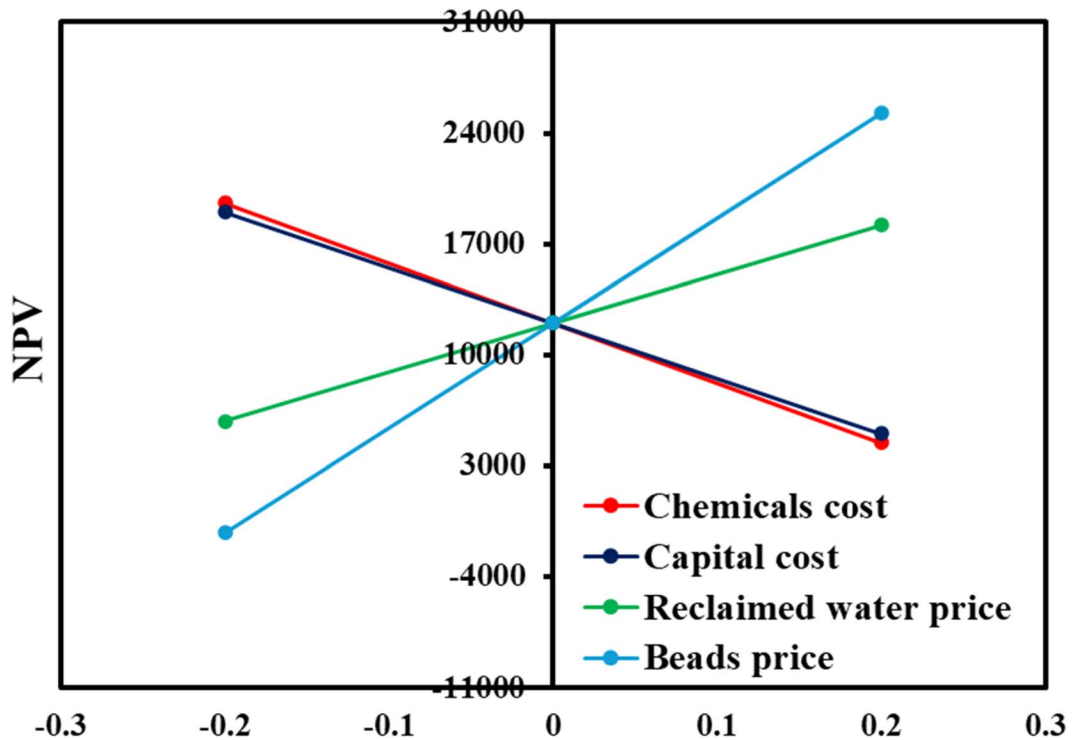

Fig. 14 Sensitivity analysis of NPV with respect to variations in chemical cost, capital cost, catalyst price, and reclaimed water price.

documented a higher total cost of 5.5 USD/m^3 for an adsorption/photocatalysis system used in industrial wastewater remediation.[109] Similarly, Alhajeri *et al.* estimated a total cost of 7.7 USD/m^3 for a photocatalytic system treating petrochemical wastewater.[113] In comparison, the total cost of the present degradation system demonstrates competitive economic performance relative to these reported technologies, supporting its cost-effectiveness and practical applicability.

4 Conclusions

Buoyant SA/WLBC/HGMs composite beads were successfully fabricated and comprehensively characterized, then applied as an efficient PI activator in a continuous-flow packed-bed photoreactor for the degradation of CBF and other pesticides (diazinon, malathion, and chlorpyrifos). Under the determined optimum conditions, TOC mineralization efficiencies of 80.27%, 66.32%, 85.94%, and 51.85% were achieved for CBF, diazinon, malathion, and chlorpyrifos, respectively. Furthermore, when the four pesticides were simultaneously present in a mixed solution (15 mg L^{-1} each), the system maintained considerable degradation efficiencies of 72.78%, 65.49%, 53.25%, and 51.88% for CBF, diazinon, malathion, and chlorpyrifos, respectively, accompanied by a TOC mineralization efficiency of 49.87%. The SA/WLBC/HGMs–PI/light system exhibited excellent reusability over five successive cycles, maintaining high CBF removal efficiencies of 94.11%, 93.89%, 93.39%, 92.87%, and 92.25%, respectively. Mechanistic investigations revealed that singlet oxygen was the predominant ROS in the degradation process, contributing more significantly than other free radicals. The proposed system operated without the formation of iodinated disinfection byproducts, highlighting its environmental safety. Furthermore, CBF was transformed into less toxic intermediate products through oxidative reactions mediated by the generated ROS. Among the tested inorganic anions (HCO_3^-, NO_3^-, SO_4^{2-}, Cl^-, and HPO_4^{2-}), HCO_3^- showed the most pronounced suppression. CBF degradation efficiency decreased slightly in real water matrices compared with deionized water, following the order: deionized water > tap water > river water > seawater > lake water; however, high CBF removal efficiencies were still achieved, demonstrating strong environmental adaptability and practical applicability in complex water matrices. From an economic perspective, the proposed treatment system for the degradation of mixed-pesticide wastewater was found to be financially viable, exhibiting a payback period shorter than the project lifetime, a positive net present value, and a profitability index of 1.3. Overall, this study recommends a low-cost, stable, and economically feasible continuous-flow photoreactor for the large-scale industrial wastewater treatment application.

Future studies should incorporate a comprehensive life cycle assessment to evaluate the overall environmental sustainability of the proposed system. In addition, assessment of the cytotoxicity of the treated effluent is recommended to confirm its environmental safety. A more in-depth elucidation of the degradation mechanism is also required, particularly through electron spin resonance analysis to directly identify reactive species. Furthermore, validation of the system using real industrial wastewater is necessary. Finally, the design, fabrication, and implementation of a larger-scale photoreactor should be pursued to facilitate practical application in industrial effluent treatment.

Author contributions

Karim Amer: investigation, methodology, data curation, formal analysis, validation, visualization, and writing – original draft. Arafat Toghan: investigation, methodology, formal analysis, data curation, visualization, validation, and writing – review & editing. Emad M. Masoud: investigation, data curation, methodology, visualization, and writing – review & editing. Magdi E. A. Zaki: investigation, methodology, validation, visualization, and writing – review & editing. Hassan Shokry: investigation, methodology, validation, visualization, and writing – review & editing. Mahmoud Samy: data curation, investigation, methodology, validation, visualization, and writing – review & editing. Mohamed Gaber: conceptualization, investigation, methodology, data curation, formal analysis, validation, visualization, writing – original draft, and writing – review & editing.

Conflicts of interest

The authors declare no conflicts of interest.

Data availability

Data will be made available on request.

Supplementary information (SI) is available. See DOI: https://doi.org/10.1039/d6ra02593e.

Acknowledgements

This work was supported and funded by the Deanship of Scientific Research at Imam Mohammad Ibn Saud Islamic University (IMSIU) (grant number IMSIU-DDRSP2602).

References

1 V. Kumar, Y. Kumar, C. Das, S. Das and S. Sen, *Chem. Eng. J.*, 2024, **499**, 155930.
2 M. Samy, M. Gar Alalm, M. Fujii and M. G. Ibrahim, *J. Water Process Eng.*, 2021, **44**, 102449.
3 A. Latief, T. Himawan and M. Mirza, *Adv. Agrochem*, 2024, **3**, 237–245.
4 A. Ccanccapa, A. Masiá, V. Andreu and Y. Picó, *Sci. Total Environ.*, 2016, **540**, 200–210.
5 C. Zhang, Y. Xu, B. Chu and X. Sun, *RSC Adv.*, 2024, **14**, 30582.
6 M. Samy, A. Gyamfi, E. Salama, M. Elkady, K. Mensah and H. Shokry, *Process Saf. Environ. Prot.*, 2023, **169**, 337–351.
7 Y. Wang, N. Lin, Y. Gong, R. Wang and X. Zhang, *Chemosphere*, 2021, **280**, 130663.
8 G. Crini and E. Lichtfouse, *Environ. Chem. Lett.*, 2019, **17**, 145–155.

9 M. Syafrudin, R. A. Kristanti, A. Yuniarto, T. Hadibarata, J. Rhee, W. A. Al-onazi, T. S. Algarni, A. H. Almarri and A. M. Al-Mohaimeed, *Int. J. Environ. Res. Public Health*, 2021, **18**, 468.
10 M. M. Gaber, A. Toghan, A. M. Eldesoky, S. A. Al-Hussain, E. M. Masoud, H. Shokry, M. Samy and M. Elkady, *Catalysts*, 2025, **15**, 1017.
11 H. Shokry, A. Toghan, M. E. A. Zaki, M. Samy, M. M. Gaber and M. Elkady, *J. Inorg. Organomet. Polym. Mater.*, 2026, 1–23.
12 M. M. Gaber, M. Samy, A. Azam and H. Shokry, *J. Environ. Chem. Eng.*, 2024, **12**, 114399.
13 S. Sujinnapram, S. Krobthong, S. Moungsrijun, C. Boonruang, N. Kaewtrakulchai, A. Eiad-Ua, K. Manatura and S. Wongrerkdee, *Mater. Today Commun.*, 2024, **40**, 109501.
14 S. Tabasum, P. P. Singh, A. Pramanik, V. Kavitha and R. Iqbal, *Top. Catal.*, 2026, **69**, 656–667.
15 M. Samy, M. Gar Alalm, M. Fujii and M. G. Ibrahim, *J. Water Process Eng.*, 2021, **44**, 102449.
16 M. Samy, A. G. Kumi, E. Salama, M. ElKady, K. Mensah and H. Shokry, *Process Saf. Environ. Prot.*, 2023, **169**, 337–351.
17 M. M. Gaber, M. Samy, E. A. El-Bestawy and H. Shokry, *Chemosphere*, 2024, **352**, 141448.
18 M. M. Gaber, H. Shokry, M. Samy and E. A. El-Bestawy, *Chemosphere*, 2024, **364**, 143245.
19 Z. Wang, Y. Zhang, T. Yuan, R. Zhang and X. Li, *Sep. Purif. Technol.*, 2026, **382**, 135846.
20 T. Elmitwalli, M. Fouad, M. Mossad and M. Samy, *J. Environ. Chem. Eng.*, 2024, **12**, 112101.
21 S. Ma, C. Zhang, Q. Wu, F. Meng, Y. Liu, H. Liu and K. Zuo, *Sep. Purif. Technol.*, 2026, **392**, 137172.
22 J. Dai, T. Cai, X. Li, M. Liu, Z. Huang and Z. Kong, *Chem. Eng. J.*, 2023, **476**, 146795.
23 H. Kim, H. Jeon, N. Yang, B. Jun, C. Min, M. Jang, J. Ye and Y. Yoon, *Chem. Eng. J.*, 2025, **523**, 168960.
24 C. Yang, Z. Yang, K. Yang, Z. Yu, Y. Zuo, L. Cheng, Y. Wang, H. Sun, G. Yu, C. Zhang and X. Li, *Sep. Purif. Technol.*, 2022, **301**, 122022.
25 M. Samy, N. Rashid, A. S. Bostaji, A. Alzahrani, H. Shokry and M. M. Gaber, *Process Saf. Environ. Prot.*, 2026, **212**, 108869.
26 P. Li, H. Lu, J. Yang, Q. Li, F. Liu, S. Huang and D. Li, *J. Water Process Eng.*, 2025, **79**, 108893.
27 Y. Yue, Q. Wang, X. Gao, X. Lu, Z. Liu and H. Ma, *J. Water Process Eng.*, 2025, **80**, 109120.
28 M. G. Dersseh, A. M. Melesse, S. A. Tilahun, M. Abate and D. C. Dagnew, in *Extreme Hydrology and Climate Variability*, Elsevier, 2019, pp. 237–251.
29 V. D. Dang, D. Quang, H. Huu, I. Rabani and C. Van Nguyen, *Chem. Eng. Sci.*, 2025, **316**, 122005.
30 W. Zou, M. Zhang, X. Zhang, D. Zhang and C. Li, *J. Environ. Chem. Eng.*, 2025, **13**, 115742.
31 M. N. Abdul-Raheem, I. O. Saheed, N. H. M. Kaus, R. Adnan, S. Thongmee, S. Shehu Imam, O. H. Hassan and S. Sagadevan, *J. Water Process Eng.*, 2025, **74**, 107826.
32 Z. Qiao, R. Sun, Y. Wu, S. Hu, X. Liu, J. Chan and X. Mi, *Environ. Res.*, 2020, **191**, 110069.
33 H. Li, X. Wang, H. Nie, Y. Xu, X. Pei and H. Cheng, *Environ. Technol. Innov.*, 2025, **38**, 104155.
34 H. gen Yang, M. Lu, X. jiao Wu, R. ting Dong, T. peng Luo and H. hua Zhong, *Chemosphere*, 2023, **339**, 139677.
35 P. Azmoon, M. Farhadian and A. Pendashteh, *Chem. Eng. J.*, 2025, **515**, 163659.
36 K. Qiao, W. Tian, J. Bai, J. Zhao, Z. Du, T. Song, M. Chu, L. Wang and W. Xie, *Environ. Technol. Innov.*, 2020, **19**, 100907.
37 J. Wu, H. Zheng, F. Zhang, R. J. Zeng and B. Xing, *Chem. Eng. J.*, 2019, **362**, 21–29.
38 Y. Li, X. Zhang, H. H. Ngo, W. Guo, T. Long, H. T. Wen and D. Zhang, *J. Memb. Sci.*, 2023, **670**, 121383.
39 M. M. Gaber, M. Abdel Rafea, H. Shokry, M. Samy, A. M. Ahmed and M. Elkady, *Catalysts*, 2025, **15**, 1049.
40 A. K. Topaloğlu, B. F. Kahraman and S. Engün, *Sustainability*, 2025, **17**, 8469.
41 H. Zeng, Y. Chen, J. Xu, S. Li, J. Wu, D. Li and J. Zhang, *Chem. Eng. J.*, 2024, **482**, 148885.
42 Y. Sukhatskiy, M. Shepida, M. Sozanskyi, Z. Znak and P. R. Gogate, *Sep. Purif. Technol.*, 2023, **304**, 122305.
43 Y. Yuan, W. Wang, M. Nie, C. Yan, P. Wang and M. Ding, *Chem. Eng. J.*, 2024, **479**, 147541.
44 H. Ying and Y. Mao, *Environ. Monit. Assess.*, 2024, **196**, 354.
45 A. Eslami, F. Mehdipour, R. Feizi, F. Ghanbari, K. Y. A. Lin, A. Bagheri and S. Madihi-Bidgoli, *Korean J. Chem. Eng.*, 2023, **40**, 882–891.
46 M. M. Gaber, M. Samy and H. Shokry, *Environ. Sci. Pollut. Res.*, 2024, **31**, 25163–25181.
47 M. Rehali, N. El Ghachtouli, S. F. Lange and R. Bouamri, *Sci. Afr.*, 2025, **27**, e02599.
48 S. Cheah, S. C. Malone and C. J. Feik, *Environ. Sci. Technol.*, 2014, **48**, 8474–8480.
49 M. M. Gaber, H. Shokry, M. Samy and E. A. El-Bestawy, *Chemosphere*, 2024, **364**, 143245.
50 Q. Chen, T. C. Zhang, L. Ouyang, S. Yuan, Q. Chen, T. C. Zhang, L. Ouyang and S. Yuan, *Molecules*, 2022, **27**, 269.
51 Y. Kassa, A. Amare, T. Nega, T. Alem, M. Gedefaw, B. Chala, B. Freyer, B. Waldmann, T. Fentie, T. Mulu, T. Adgo, G. Ayalew, M. Adugna and D. Tibebe, *Sci. Rep.*, 2025, **15**, 1820.
52 D. Losacco, C. Campanale, M. Tumolo, V. Ancona, C. Massarelli and V. F. Uricchio, *Sustainability*, 2022, **14**, 11985.
53 M. M. Gaber, A. Toghan, H. Shokry and M. Samy, *RSC Adv.*, 2025, **15**, 31522–31538.
54 J. Raissouni, K. Draoui, A. A. Aghzzaf, R. Cela-Dablanca, A. Barreiro, M. J. Fernández-Sanjurjo, A. Núñez-Delgado and E. Álvarez-Rodríguez, *J. Environ. Manage.*, 2025, **374**, 123952.
55 J. Raissouni, K. Draoui, A. A. Aghzzaf, R. Cela-Dablanca, A. Barreiro, M. J. Fernández-Sanjurjo, A. Núñez-Delgado and E. Álvarez-Rodríguez, *J. Hazard. Mater.*, 2025, **496**, 139267.

56 A. Ray, A. Banerjee and A. Dubey, *Int. J. Environ. Agric. Biotech.*, 2020, **13**, 864.
57 T. K. Das, Q. Scott and A. N. Bezbaruah, *J. Environ. Chem. Eng.*, 2025, **13**, 116815.
58 E. J. Lee and J. W. Lee, *Environ. Technol. Innov.*, 2025, **40**, 104660.
59 S. Mohan, M. Vellakkat and R. U, *J. Indian Chem. Soc.*, 2026, **103**, 102341.
60 R. Aali, H. Azari, H. Pasalari, K. Yaghmaeian, M. Yousefi, A. Azari, A. R. Yari, N. Sharifi, H. Kamani and M. Dowlati, *Sci. Rep.*, 2025, **15**, 25013.
61 X. Tang, S. Ma, S. Xu, C. Pei, T. Dong, Q. Yang, Y. Huang, J. Wang, B. Gao, D. Hua, B. Dang and S. Zhan, *Chem. Eng. J.*, 2023, **471**, 144765.
62 P. Gao, Y. Su, Y. Xie, J. Wang, G. Zeng and D. Sun, *Sustainability*, 2025, **17**, 9199.
63 Y. Mao, Y. Xu and H. Ying, *Environ. Earth Sci.*, 2024, **83**, 548.
64 E. A. El-Bestawy, M. Gaber, H. Shokry and M. Samy, *Environ. Res.*, 2023, **229**, 115987.
65 M. M. Gaber, N. Rashid, A. Alzahrani and F. Alanazi, *J. Environ. Chem. Eng.*, 2025, **13**, 116031.
66 K. Hou, Z. Pi, F. Yao, B. Wu, L. He, X. Li, D. Wang, H. Dong and Q. Yang, *Chem. Eng. J.*, 2021, **407**, 127078.
67 A. Balakrishnan, F. P. Mathew, M. Tom Joseph, M. M. Varghese, K. S. Aryamol, M. Chinthala, N. Rajamohan and B. Weng, *J. Mater. Chem. A Mater.*, 2026, **14**, 5473–5519.
68 Y. Shi, C. Ma, T. Zhang, Y. Sun and G. Ding, *Catal. Lett.*, 2024, **154**(11), 5906–5920.
69 T. B. Nguyen, N. Mariappan, C. W. Chen, X. T. Bui, T. D. Pham and C. Di Dong, *J. Water Process Eng.*, 2025, **76**, 108154.
70 G. Lu, X. Li, W. Li, Y. Liu, N. Wang, Z. Pan, G. Zhang, Y. Zhang and B. Lai, *J. Hazard. Mater.*, 2024, **461**, 132696.
71 W. Zou, M. Zhang, X. Zhang, D. Zhang, C. Li, L. Zhong, W. Guo and H. H. Ngo, *J. Environ. Chem. Eng.*, 2025, **13**, 115742.
72 W. Zou, M. Zhang, X. Zhang, D. Zhang, C. Li, L. Zhong, W. Guo and H. H. Ngo, *J. Water Process Eng.*, 2025, **69**, 106723.
73 P. Xiao, X. Yi, M. Wu, X. Wang, S. Zhu, B. Gao, Y. Liu and H. Zhou, *J. Hazard. Mater.*, 2022, **424**, 127692.
74 L. He, L. Lv, S. C. Pillai, H. Wang, J. Xue, Y. Ma, Y. Liu, Y. Chen, L. Wu, Z. Zhang and L. Yang, *Sci. Total Environ.*, 2021, **783**, 146974.
75 N. A. Rajput, M. Laghari, H. ur R. Mangio and R. K. Soothar, *Bioresour. Technol. Rep.*, 2024, **26**, 101818.
76 Y. Chen, X. Yuan, L. Jiang, Y. Zhao, H. Chen, Z. Shangguan, C. Qin and H. Wang, *Chem. Eng. J.*, 2023, **457**, 141147.
77 X. Zhang, M. Kamali, T. Uleners, J. Symus, S. Zhang, Z. Liu, M. E. V. Costa, L. Appels, D. Cabooter and R. Dewil, *Chem. Eng. J.*, 2022, **449**, 137680.
78 D. Yu and Y. Pei, *J. Environ. Manage.*, 2022, **321**, 115890.
79 Y. N. Kanafin, P. Abdirova, D. Kanafina, E. Arkhangelsky, G. Z. Kyzas and S. G. Poulopoulos, *Catalysts*, 2023, **13**, 25.
80 Q. Jamil, B. Žener, U. Putar and L. Matoh, *Heliyon*, 2024, **10**, e40019.
81 L. Chen, H. Huang, X. Zhang, W. Tang, J. He and Y. Yang, *J. Water Process Eng.*, 2024, **65**, 105879.
82 L. Yang, F. Yang, H. Zhang, H. Zhou, M. Luo, Y. Liu, C. Zhao, L. Zheng and B. Lai, *J. Hazard. Mater.*, 2023, **454**, 131479.
83 L. He, Y. Shi, Y. Chen, S. Shen, J. Xue, Y. Ma, L. Zheng, L. Wu, Z. Zhang and L. Yang, *Sep. Purif. Technol.*, 2022, **288**, 120703.
84 S. Ye, M. Yan, X. Tan, J. Liang, G. Zeng, H. Wu, B. Song, C. Zhou, Y. Yang and H. Wang, *Appl. Catal. B*, 2019, **250**, 78–88.
85 Y. Xiong, X. Tang, Y. Liu, W. Li, Y. He, Y. Deng, Z. Lin and Y. Zhou, *Sep. Purif. Technol.*, 2024, **333**, 125813.
86 H. Sun, G. Geng, S. Lin, D. Wu, S. Yu and C. Gao, *J. Water Process Eng.*, 2025, **69**, 106687.
87 P. Wijekoon, P. A. Koliyabandara, A. T. Cooray, S. S. Lam, B. C. L. Athapattu and M. Vithanage, *Chem. Eng. J. Adv.*, 2023, **14**, 100452.
88 C. Y. Hu, Z. Y. Dong, Z. Y. Dong, Y. H. Wu, S. J. Ji, L. L. Hu, X. Y. Yang, H. Liu and B. Xu, *Sep. Purif. Technol.*, 2024, **342**, 127023.
89 W. Xu, Q. Wang, J. He, F. Liu, X. Yan and Y. Xu, *Separations*, 2024, **11**, 274.
90 L. Yang, L. He, Y. Ma, L. Wu, L. Zheng, J. Wang, Y. Chen, Y. Li and Z. Zhang, *Sep. Purif. Technol.*, 2022, **289**, 120746.
91 X. Wang, W. Tang, L. Jiang, J. Feng, J. Yang, S. Zhou, W. Li, X. Yuan, H. Wang, J. Wang and Y. Bu, *Chem. Eng. J.*, 2023, **471**, 144521.
92 W. Duan, M. Zhang and R. Zhou, *Water Sci. Technol.*, 2024, **89**, 212–224.
93 K. Zhang, Y. Xie, Z. Ye, W. Zhang, Q. Zhang, X. Yu and M. Feng, *Chem. Eng. J.*, 2023, **461**, 141879.
94 S. Zang, W. Qiu, Y. Jiang, S. Chen, Y. Qiao, B. Zhang, Z. Yang, X. Wang and J. Ma, *Environ. Sci. Technol.*, 2026, **60**, 2137–2147.
95 K. Zhang, S. Zhang, C. Ye, R. Ou, H. Zeng, X. Yu and M. Feng, *Chem. Eng. J.*, 2023, **451**, 138642.
96 L. A. Lu, Y. S. Ma, M. Kumar and J. G. Lin, *Chem. Eng. J.*, 2011, **166**, 150–156.
97 H. Zouggari, F. Z. Mahir, A. M. Diez, R. Djellabi, M. A. Sanromán, A. Albourine and M. Pazos, *Chem. Eng. J.*, 2026, **529**, 173054.
98 H. Zouggari, F. Z. Mahir, A. M. Diez, R. Djellabi, M. A. Sanromán, A. Albourine and M. Pazos, *Chem. Eng. J.*, 2026, **529**, 173054.
99 M. M. Gaber, A. Azam, A. Alzahrani, F. Alanazi, H. Shokry and M. Samy, *J. Environ. Manage.*, 2025, **395**, 127712.
100 Y. Yang, Z. Kang, G. Xu and Y. Yu, *J. Hazard. Mater.*, 2024, **480**, 135803.
101 X. Wang, P. Zhang, S. Meng, C. Zhou, Z. Xiong, C. He, Y. Liu, H. Zhang, P. Zhou and B. Lai, *Sep. Purif. Technol.*, 2025, **354**, 129186.
102 Q. Liu, L. Zhou, L. Liu, J. Li, S. Wang, H. Znad and S. Liu, *Compos. B Eng.*, 2020, **200**, 108345.
103 W. Xu, X. Zheng, Z. Shangguan, J. Qu and W. Zhang, *Chem. Eng. J.*, 2023, **464**, 142562.

104 J. Qian, X. Mi, Z. Chen, W. Xu, W. Liu, R. Ma, Y. Zhang, Y. Du and B. J. Ni, *J. Clean. Prod.*, 2023, **405**, 137023.
105 L. He, S. Yang, S. Shen, Y. Ma, Y. Chen, J. Xue, J. Wang, L. Zheng, L. Wu, Z. Zhang and L. Yang, *J. Hazard. Mater.*, 2022, **434**, 128860.
106 D. Prato-Garcia, P. J. Espinoza-Montero, A. Talbi, S. Merouani and A. Dehane, *Processes*, 2025, **13**, 1487.
107 J. Sheng, S. Guo, C. Yuan, X. Nie, P. Cui and H. Jiang, *Chem. Eng. J.*, 2023, **466**, 143158.
108 J. Wen, L. Zhou, Q. Tang, X. Xiao and S. Sun, *Ecotoxicol. Environ. Saf.*, 2023, **262**, 115133.
109 B. Emmanuel, A. Abdelhaleem and M. Nasr, *J. Water Process Eng.*, 2026, **81**, 109345.
110 J. C. G. Sousa, A. R. Ribeiro, M. O. Barbosa, M. F. R. Pereira and A. M. T. Silva, *J. Hazard. Mater.*, 2018, **344**, 146–162.
111 K. F. Ngulube, A. Abdelhaleem, M. Fujii and M. Nasr, *J. Water Process Eng.*, 2024, **64**, 105605.
112 D. Dadebo, M. G. Ibrahim, M. Fujii and M. Nasr, *J. Environ. Chem. Eng.*, 2026, **14**, 121251.
113 N. S. Alhajeri, A. Tawfik, M. Nasr and A. I. Osman, *Chemosphere*, 2024, **352**, 141476.